UC Berkeley

UC Berkeley Previously Published Works

Title

Manipulating chiral spin transport with ferroelectric polarization

Permalink

https://escholarship.org/uc/item/62n598cg

Journal

Nature Materials, 23(7)

ISSN

1476-1122

Authors

Huang, Xiaoxi

Chen, Xianzhe

Li, Yuhang

et al.

Publication Date

2024-07-01

DOI

10.1038/s41563-024-01854-8

Copyright Information

This work is made available under the terms of a Creative Commons Attribution-NonCommercial-NoDerivatives License, available at https://creativecommons.org/licenses/by-nc-nd/4.0/

Peer reviewed

eScholarship.org Powered by the California Digital Library
University of California

Manipulating chiral-spin transport with ferroelectric polarization

Xiaoxi Huang[1,†], Xianzhe Chen[1,2,†,*], Yuhang Li[3,†], John Mangeri[4,†], Hongrui Zhang[1], Maya Ramesh[5], Hossein Taghinejad[6], Peter Meisenheimer[1], Lucas Caretta[1], Sandhya Susarla[2,7], Rakshit Jain[8,9], Christoph Klewe[10], Tianye Wang[6], Rui Chen[1], Cheng-Hsiang Hsu[2,11], Isaac Harris[6], Sajid Husain[1,2], Hao Pan[1], Jia Yin[12], Padraic Shafer[10], Ziqiang Qiu[6], Davi R. Rodrigues[13], Olle Heinonen[14], Dilip Vasudevan[12], Jorge Íñiguez[4,15], Darrell G. Schlom[5], Sayeef Salahuddin[2,11], Lane W. Martin[1,2], James G. Analytis[6], Daniel C. Ralph[8,9], Ran Cheng[3,16], Zhi Yao[12], and Ramamoorthy Ramesh[1,2,6,*]

[1]*Department of Materials Science and Engineering, University of California, Berkeley, CA 94720, USA*
[2]*Materials Sciences Division, Lawrence Berkeley National Laboratory, CA 94720, USA*
[3]*Department of Electrical and Computer Engineering, University of California, Riverside, CA 92521, USA*
[4]*Materials Research and Technology Department, Luxembourg Institute of Science and Technology (LIST), Avenue des Hauts-Fourneaux 5, L-4362, Esch/Alzette, Luxembourg*
[5]*Department of Materials Science and Engineering, Cornell University, Ithaca, NY 14853, USA.*
[6]*Department of Physics, University of California, Berkeley, CA 94720, USA*
[7]*School for Engineering of Matter, Transport and Energy, Arizona State University, Tempe, AZ 85281, USA*
[8]*Department of Physics, Cornell University, Ithaca, NY 14853, USA*
[9]*Kavli Institute at Cornell for Nanoscale Science, Ithaca, NY 14853, USA*
[10]*Advanced Light Source, Lawrence Berkeley National Laboratory, Berkeley, CA 94720, USA*
[11]*Department of Electrical Engineering and Computer Sciences, University of California, Berkeley, CA 94720, USA*
[12]*Applied Mathematics and Computational Research Division, Lawrence Berkeley National Laboratory, CA 94720, USA*
[13]*Department of Electrical Engineering, Politecnico di Bari, Via Edoardo Orabona, 4, 70126 Bari BA, Italy*
[14]*Materials Science Division, Argonne National Laboratory, 9700 S Cass Ave, Lemont, IL 60439, USA*
[15]*Department of Physics and Materials Science, University of Luxembourg, 41 Rue du Brill, Belvaux L-4422, Luxembourg*
[16]*Department of Physics and Astronomy, University of California, Riverside, California 92521, USA*

A collective excitation of the spin structure in a magnetic insulator can transmit spin-angular momentum with negligible dissipation[1–5]. This quantum of a spin wave, introduced more than nine decades ago[6], has always been manipulated through magnetic dipoles[7–10], (*i.e.*, time-reversal symmetry). Here, we report the experimental observation of chiral-spin transport in multiferroic $BiFeO_3$, where the spin transport is controlled by reversing the ferroelectric polarization (*i.e.*, spatial inversion symmetry). The ferroelectrically controlled magnons produce an ratio of up to 18% rectification at room temperature. The spin torque that the magnons in $BiFeO_3$ carry can be used to efficiently switch the magnetization of adjacent

* E-mail: xzchen@berkeley.edu, rramesh@berkeley.edu
Present and permanent address of Olle Heinonen: Seagate Technology, 7801 Computer Avenue, Bloomington MN 55435

magnets, with a spin-torque efficiency being comparable to the spin Hall effect in heavy metals. Utilizing such a controllable magnon generation and transmission in $BiFeO_3$, an all-oxide, energy-scalable logic is demonstrated composed of spin-orbit injection, detection, and magnetoelectric control. This observation opens a new chapter of multiferroic magnons and paves an alternative pathway towards low-dissipation nanoelectronics.

Intense studies of spin current transport in magnetic insulators[4,11–14] have opened various avenues for research on spintronics[15–21] and their potential use in low-power applications[13]. This trend has also triggered renewed interest in magnon physics, which can be controlled via time-reversal-symmetry design (*e.g.*, magnetic domain walls[7], spin Hall currents[8,9], static magnetic fields[10]). On the other hand, recent works have shown that broken inversion symmetry and the resulting Dzyaloshinskii-Moriya interaction (DMI) have profound influence on magnon transport in non-centrosymmetric magnets[22–25]. In this spirit, multiferroics are potentially of great interest, since they display broken inversion symmetry and a ferroelectric polarization that can be switched by the application of an electric field, which in turn allows for control of the magnetism and, potentially, the magnons. The idea that multiferroics could be promising candidates for magnonic manipulation has been considered for some time[13,26], but despite this early interest, observation and manipulation of magnon transport in multiferroics - that is, the capability to manipulate spin transport via ferroelectric polarization reversal and resultant DMI switching- remain elusive.

Here, we demonstrate non-volatile, bistable spin transport in multiferroic $BiFeO_3$ upon reversing the ferroelectric polarization. $BiFeO_3$ is a model multiferroic that exhibits multiple order parameters (*i.e.*, antiferromagnetism and ferroelectricity) and intrinsic magnetoelectric coupling of these coexisting order parameters[27,28]. In the bulk, $BiFeO_3$ possesses a rhombohedrally distorted perovskite structure in which a spin cycloid [29]is formed with a period length of ~ 64 nm [30,31] and a Néel temperature of ~ 643 K [32]. The DMI in $BiFeO_3$ thin films can influence the spin cycloid order[13,33,34]. At the same time, $BiFeO_3$ thin films possess robust ferroelectricity, with a Curie temperature ~ 1100 K and a large polarization > 90 μ C/cm^2 [35]. In turn, $BiFeO_3$ exhibits outstanding magnetoelectric properties which have made it the focus of numerous studies hoping to utilize it as a platform to achieve low-energy (low-voltage) memory devices (*e.g.*, deterministic switching of adjacent ferromagnets[36]). Specifically, achieving control over changing the magnetization states through ferroelectric polarization switching has always been a keen pursuit in these studies.

As illustrated in Fig. 1a, a spin cycloid propagating along $\boldsymbol{q} = [1\bar{1}0]$ is revealed by Nitrogen-Vacancy diamond magnetometry measurements (Extended Data Fig. 1), which is in good agreement with the pioneering work of Gross et al[30,31]. The formation of spin cycloid has been explained in terms of a Lifshitz-like invariant[37] which, in the continuum limit, amounts to an effective DMI vector $\boldsymbol{D}_0$ perpendicular to both the ferroelectric polarization $\boldsymbol{P}$ (along $[111]$) and the spin cycloid propagating direction $\boldsymbol{q}$. In $BiFeO_3$, there is another intrinsic DMI characterized by a global DMI vector parallel to $\boldsymbol{P}$, which is responsible for the small magnetization $\boldsymbol{m}$ everywhere perpendicular to the Néel vector $\boldsymbol{L}$. Due to this, the magnon band is circularly polarized (Extended data Fig. 2).

Previous studies have confirmed that the latter mechanism is much weaker so that the spin texture is dominated by $\boldsymbol{D_0}$[37,38]. A reversal of $\boldsymbol{P}$ is accompanied by the reversal of the octahedral antiphase tilts[36], which in turn flips the direction of $\boldsymbol{D}_0$[34,37]. In addition, the asymmetric gates, the existence of ferroelectric domain walls[39], and other asymmetries of external origins generate a built-in potential that induces an additional DMI vector $\delta\boldsymbol{D}$, which remains the same under the reversal of $\boldsymbol{P}$. Consequently, the total DMI vector $\boldsymbol{D}_0 + \delta\boldsymbol{D}$ undergoes a non-180° switching, leading to a slight rotation of the propagation direction $\boldsymbol{q}$. A flexoelectric polarization induced by the strain gradient may also exist[40]; however, its typical value is orders of magnitude smaller than the intrinsic ferroelectric pololarization in $BiFeO_3$. To intuitively understand the ferroelectric control of magnon spin current, we define the hybrid product $(\boldsymbol{D}_0 \times \delta\boldsymbol{D}) \cdot \boldsymbol{K}$ where $\boldsymbol{K}$ is the magnon wave vector (in the thickness direction). It is well-known that the nonreciprocal propagation is allowed not only in magnons but also electrons, electromagnetic waves when they go through materials such as multiferroic materials that host broken time reversal and space inversion symmetry simultaneously. As illustrated in Fig. 1a, reversing $\boldsymbol{P}$ necessarily flips the sign of $(\boldsymbol{D}_0 \times \delta\boldsymbol{D}) \cdot \boldsymbol{K}$, hence the chirality of these three vectors.

Because the thickness of $BiFeO_3$ is much smaller than the spatial period ($\sim$64 nm) of the spin cycloid, we can ignore any spin texture or magnetic inhomogeneity along the magnon wave vector $\boldsymbol{K}$. Then, the transmitted spin current can be phenomenologically expressed as[15]

$$J_s = \frac{G_L}{\mathcal{S}} \int d\mathbf{r}^2 [\boldsymbol{L}(\boldsymbol{r}) \cdot \boldsymbol{s}]^2 + \frac{G_m}{\mathcal{S}} \int d\mathbf{r}^2 [\boldsymbol{m}(\boldsymbol{r}) \cdot \boldsymbol{s}]^2, \tag{1}$$

where G_L (G_m) is the phenomenological spin conductance of the Néel vector (total magnetization), $\boldsymbol{s} = \hat{y}$ is the polarization of spin injection from the top gate and $\mathcal{S}$ is the area of the film. As mentioned above, when the total DMI vector undergoes a non-180° switching, the spin cycloid profile functions $\boldsymbol{L}(\boldsymbol{r})$ and $\boldsymbol{m}(\boldsymbol{r})$ are modulated by $\boldsymbol{P}$ in a non-trivial way. As calculated in the Supplemental Materials, the resulting spin current J_s can be substantially different before and after the reversal of $\boldsymbol{P}$. To quantify this difference, we define the rectification ratio as

$$\xi = \frac{J_s(-\boldsymbol{P}) - J_s(\boldsymbol{P})}{J_s(-\boldsymbol{P}) + J_s(\boldsymbol{P})} \tag{2}$$

and plot it against the orientation of the extrinsic $\delta\boldsymbol{D}$ relative to the intrinsic $\boldsymbol{D}_0$ (along $[\bar{1}\bar{1}2]$) in Fig. 1b, where we have marked the experimental value (to be explained below) $\xi = 0.18$.

Based on the predicted potential for chiral-magnon control in $BiFeO_3$, a demonstration of a scalable magnetoelectric spin-orbit logic was investigated. A schematic of this idea is illustrated in Fig. 1d. An electric field is set up in the magnetoelectric capacitor in the $-z$ direction, resulting in the vertical component of the ferroelectricity switching from the z to the $-z$ direction. To read the polarization state, a supply voltage is applied into the top spin-orbit coupled (SOC) channel (*e.g.*, $SrIrO_3$ which has a relatively large spin Hall angle[41]) in the $+x$ direction, causing the excitation of magnons in the $BiFeO_3$ via the spin current from the SOC material. The readout of the state of the switch is then enabled by the inverse spin Hall effect using the bottom $SrIrO_3$ channel[42], where

the current direction is along the x direction. Owing to the magnon propagation with bistable rectification, the output voltage could acquire two stable states, rendering the buffer function of a logic gate. Especially, as compared with the first magneto-electric, spin-orbit (MESO) device proposal[43], this design makes use of antiferromagnetic magnon to gauge the antiferromagnetism inside the multiferroic itself instead of relying on the adjacent ferromagnet coupled to the multiferroic (Extended Data Fig. 3). Early efforts on the elimination of the ferromagnet have been devoted to the electric-field controlled spin-orbit interaction[44,45], e.g. Rashba effect in two-dimensional electron gas systems[46,47]. The elimination of the ferromagnet simplifies the readout architecture; furthermore, the implementation of antiferromagnets can favor ultrafast operations frequency up to THz.

To experimentally explore the controllable spin transmission enabled by the ferroelectric switch in $BiFeO_3$, we first characterized the strength of spin transmission via magnons in the heterostructures of the form $La_{0.7}Sr_{0.3}MnO_3$/$BiFeO_3$ /$SrIrO_3$ (Methods, Extended Data Fig. 4,5). We performed the measurement using a well-established technique namely spin-torque ferromagnetic resonance (ST-FMR)[41,48](Fig. 2a), launching the spin current using the large spin Hall effect of $SrIrO_3$ and detecting the spin torque applied to the magnetic $La_{0.7}Sr_{0.3}MnO_3$ layer[49]. An example ST-FMR spectrum, composed of both symmetric and anti-symmetric components, is shown (Fig. 2b) and indicates the successful detection of the spin currents carried by magnons through the $BiFeO_3$. To manipulate the orientation of the ferroelectric polarization, an external electric field was applied along the out-of-plane $[001]$ to set the ferroelectric polarization of the $BiFeO_3$ as illustrated (top panel, Fig. 2c, in which the top $SrIrO_3$ and bottom $La_{0.7}Sr_{0.3}MnO_3$ layers serve as the two electrodes sandwiching the ferroelectric). Specifically, upward- (downward-) pointing polarization (180° switching) can be achieved by applying negative (positive) voltage larger than the coercivity of the $BiFeO_3$ on the top $SrIrO_3$ layer (bottom panel, Fig. 2c)[42]. After poling the $BiFeO_3$ in each individual device to the desired polarization state, we then deposited platinum contacts onto the devices (contacting both the $SrIrO_3$ and $La_{0.7}Sr_{0.3}MnO_3$ layers) and performed ST-FMR measurements on the poled devices. By adopting an established analysis method (Methods), the SOT efficiency for the damping-like (DL) torque (symmetric component) is evaluated and summarized (Fig. 2d). We observe that the SOT efficiency can be set at a high value by negative (upward polarization) or at a low value by positive (downward polarization) voltages, indicating the presence of bistable high/low spin transport in $BiFeO_3$. This polarization-dependent spin transmission of $BiFeO_3$ is also verified by interfacial engineering (Extended Data Fig. 6), time-resolved X-ray ferromagnetic resonance (Extended Data Fig. 7) and FMR measurements (Extended Data Fig. 8, 9). The blocking temperature of exchange bias between $La_{0.7}Sr_{0.3}MnO_3$ and $BiFeO_3$ is well below room temperature[50], and the absence of exchange bias is also confirmed by our magneto-optic Kerr effect measurements (Extended Data Fig. 10), ruling out the possible contribution from exchange bias on the tuning of spin transmission. It is worthwhile to note that the stability of the ferroelectric polarization reveals another crucial advantage associated with spintronics produced in this manner – non-volatility. By setting the polarization direction, high and low SOT efficiencies of 0.33 and 0.23 can be achieved, showing a high/low ratio of 0.18. Furthermore, the ferroelectric polarization controlled spin transmission in $BiFeO_3$ is confirmed by ST-FMR measurements on samples with

opposite polarizations set by different interface terminations[51] (Extended Data Fig. 6). This is consistent with our theoretical predictions that the polarization state influences magnon propagation and a spin transmission modulation can be achieved upon ferroelectric polarization switching. Further, from the aforementioned experiments it can be inferred that the spin transmission is favorable when the magnon wave vector is anti-parallel to the z-component of the polarization $\boldsymbol{P}$.

To corroborate the presence of a magnon transmission modulation in $BiFeO_3$, magnetization switching experiments were carried out to serve as a direct demonstration of the strength of the spin torques under ferroelectric polarization modulation. Here, we investigate deterministic magnetization switching of a $SrRuO_3$ layer with perpendicular magnetic anisotropy (PMA) by the spin torque carried by the $BiFeO_3$. Current-induced magnetization switching measurements were carried out for $SrRuO_3$ (5 nm)/$BiFeO_3$ (25 nm)/$SrIrO_3$ (10 nm) heterostructure with $BiFeO_3$ polarized to either upward or downward orientations (Fig. 3a). The switching schematic is demonstrated (Fig. 3a). The magnetic switching was detected by the anomalous Hall effect in the $SrRuO_3$ layer, in which magnetic moments lying on the positive and negative directions can be distinguished by positive and negative values of anomalous Hall resistance. By sweeping an external magnetic field in the out-of-plane direction (Fig. 3b), a hysteretic loop is developed for anomalous Hall resistance ($\boldsymbol{R}_{XY}$), when the external magnetic field exceeds the coercivity of $SrRuO_3$(Fig. 3c). Furthermore, $\boldsymbol{R}_{XY}$ as a function of magnetic field was repeated at temperatures from 20 K to 80 K, confirming the high quality of our heterostructure, and no shift in the hysteretic loop with respect to zero magnetic field is observed, indicating the absence of exchange bias effect between ferromagnetic $SrRuO_3$ and antiferromagnetic $BiFeO_3$. Then magnetization switching measurements were performed in the same device at $70K$, and $\boldsymbol{R}_{XY}$ as a function of current pulses was recorded (3d). Notably, a switching of magnetization was observed by both positive and negative currents, when the magnitudes of current pulses exceed the magnitude of critical switching current, and a saturation of $\boldsymbol{R}_{XY}$ is observed with large current pulses, excluding the possible participation of thermal effects in the switching measurements. Moreover, no magnetization switching is observed at zero assisting magnetic field and the switching chirality can be changed by the reversal of polarity of assisting magnetic fields, ruling out the possibility that the magnetization switching is caused by current-induced Oersted field. To further corroborate our observation of ferroelectric polarization-controlled spin transport with ST-FMR, ferroelectric polarization-dependent magnetization switching measurements were carried out. To start with, the polarization of $BiFeO_3$ was switched to either an upward or downward orientation by an external electric field, prior to the deposition of Pt electrodes that simultaneously contact both the top $SrIrO_3$ and bottom $SrRuO_3$ layers. An example IV curve during the ferroelectric polarization switching measurements is displayed in Fig. 3e, in which the switching of ferroelectric polarization is associated with current peaks in Fig. 3e. Then, the same magnetization switching measurements were conducted on devices with distinct ferroelectric polarization states. A typical switching loop for heterostructures with upward (downward) polarization is displayed in red (blue) solid spheres in Fig. 3f. Strikingly, distinct critical switching currents for upward and downward polarization were observed in both positive and negative current directions. The critical switching currents at different assisting magnetic fields for upward and downward polarization are summarized in Fig. 3g, where upward

polarization shows a smaller switching current than downward polarization statistically. Therefore, two conclusions can be drawn based on our experimental observations. First, $BiFeO_3$ has the capability to carry spin information via antiferromagnet magnons, and the spin torque arising from $BiFeO_3$ is sufficient to switch the magnetization of $SrRuO_3$. More importantly, the spin transmission in $BiFeO_3$ is controlled by ferroelectric polarization, and the smaller critical switching current density for the upward polarization corresponds to a higher spin transmission, in good agreement with the ferroelectric polarization controlled-SOT efficiency study with the ST-FMR technique. The current-induced magnetization switching measurements reinforce the idea that the upward polarization is favorable for magnon transmission in vertical transport.

We further investigated the experimental demonstration of MESO via electrically controllable spin transport using a lateral nonlocal measurement. A schematic of the nonlocal measurement is provided (Fig. 4a); it consists of spin-orbit input and output via parallel source and detector wires, as well as magnetoelectric control. Fig. 4b illustrates well-ordered 71° ferroelectric domains, showing the high quality of the $BiFeO_3$ films. A nonlocal, quasi-static measurement was performed (Fig. 4c), varying the magnitude of the electric-field pulse applied in-plane across the channel from negative to positive and back again, and after each pulse measuring (over 100 seconds) non-local voltage signals due to magnon transport between the source and detector wires (Methods). We observe a butterfly-shaped and hysteretic response in the magnon current launched by the spin Hall effect (first-harmonic voltage, Fig. 4c) and the magnon current launched thermally by the local spin Seebeck effect, respectively (second-harmonic voltage, Fig. 4d), in which the coercive fields match each other. Note that the first harmonic asymmetric butterfly shape also consists of a hysteresis, which is induced with a non-perfect 180 degree switching of spin cycloid plane. Besides, the electric field modulations of the output voltage can be obtained with dc methods, which can minimize the inductive and capacitive effect (Extended Data Fig. 11,12,13,14). Figure 4e presents measurements of the magnitude of these spin-transport signals as a function of channel spacing between the source and detector wires from 500 nm to 4 μm. The open squares reflect the magnitude of the signals associated with spin currents launched by the spin Hall effect (first harmonic voltage) and the red circles reflect signals launched thermally by the spin Seebeck effect (second harmonic voltage). Remarkably, the output voltage detected in $BiFeO_3$/$SrIrO_3$ stacks ($\sim 1\ \mu$V) is approximately one order of magnitude larger than the counterparts in $BiFeO_3$/Pt ($\sim 0.1\ \mu$V)[52], which is supported by the large spin-torque efficiency of $SrIrO_3$ previously observed with the ST-FMR measurement [41,53] and the controlled nonlocal measurements of $NiFe_2O_4$/Pt and $NiFe_2O_4$/$SrIrO_3$ (Extended Data Fig. 15,16). The spacing dependence for both types of signals in $BiFeO_3$ fits well to the expectation for diffusive magnon propagation[54]

$$R_{\mathrm{nl}} = \frac{C}{\lambda} \frac{\exp(d/\lambda)}{1 - \exp(2d/\lambda)} \tag{3}$$

with effective diffusion lengths $\sim 0.17\ \mu$m (first harmonic) and $\sim 0.25\ \mu$m (second harmonic).

Using this result and the spin-torque efficiencies obtained above (Extended Data Fig. 5), we can calculate the inverse-spin-Hall output voltage that would be obtained for a vertical geometry

with $BiFeO_3$ thicknesses of 10 and 15 nm using[55]

$$V_{\mathrm{ISHE}} = \frac{\theta_{\mathrm{SOT}} \lambda_{\mathrm{SD}} \tanh(\frac{t_{\mathrm{SIO}}}{2\lambda_{\mathrm{SD}}}) L}{t_{\mathrm{SIO}} \sigma_{\mathrm{SIO}}} J_{\mathrm{S}} \tag{4}$$

where we use the values θ_{SOT} = 0.4 is the spin-torque efficiency, $\lambda_{\mathrm{SD}} = 1.4$ nm [56] is the spin-diffusion length of $SrIrO_3$, $t_{\mathrm{SIO}} = 10$ nm is the thickness, $\sigma_{\mathrm{SIO}} = 1 \times 10^5\ \Omega^{-1} m^{-1}$ is the conductivity, $L = 10$ nm is the wire length. The output voltage is on the order of 10 mV, which is approaching the MESO target voltage of 100 mV. A prototypical magnon-mediated MESO logic device and its circuit modeling utilizing this ferroelectrically controlled magnon propagation are shown in Extended Data Fig. 5. This observation sheds light on implementing multiferroics as the potential spin carriers and opens new possibilities of energy-efficient magnonic spin-logic devices.

References

1. Kruglyak, V. V., Demokritov, S. O. & Grundler, D. Magnonics. *J. Phys. D: Appl. Phys.* **43**, 264001 (2010).

2. Lenk, B., Ulrichs, H., Garbs, F. & Münzenberg, M. The building blocks of magnonics. *Phys. Rep.* **507**, 107–136 (2011).

3. Khitun, A., Bao, M. & Wang, K. L. Magnonic logic circuits. *J. Phys D: Appl. Phys.* **43**, 264005 (2010).

4. Kajiwara, Y. *et al.* Transmission of electrical signals by spin-wave interconversion in a magnetic insulator. *Nature* **464**, 262–266 (2010).

5. Chumak, A. V., Vasyuchka, V. I., Serga, A. A. & Hillebrands, B. Magnon spintronics. *Nature Phys.* **11**, 453–461 (2015).

6. Bloch, F. Zur theorie des ferromagnetismus. *Zeitschrift für Physik* **61**, 206–219 (1930).

7. Han, J., Zhang, P., Hou, J. T., Siddiqui, S. A. & Liu, L. Mutual control of coherent spin waves and magnetic domain walls in a magnonic device. *Science* **366**, 1121–1125 (2019).

8. Hamadeh, A. *et al.* Full control of the spin-wave damping in a magnetic insulator using spin-orbit torque. *Phys. Rev. Lett.* **113**, 197203 (2014).

9. Zhou, Y. *et al.* Piezoelectric strain-controlled magnon spin current transport in an antiferromagnet. *Nano Lett.* (2022).

10. Demokritov, S. O. *et al.* Tunneling of dipolar spin waves through a region of inhomogeneous magnetic field. *Phys. Rev. Lett.* **93**, 047201 (2004).

11. Wang, H., Du, C., Hammel, P. C. & Yang, F. Antiferromagnonic spin transport from $Y_3Fe_5O_{12}$ into NiO. *Phys. Rev. Lett.* **113**, 097202 (2014).

12. Chen, X. Z. *et al.* Antidamping-torque-induced switching in biaxial antiferromagnetic insulators. *Phys. Rev. Lett.* **120**, 207204 (2018).

13. Wang, J. *et al.* Epitaxial $BiFeO_3$ multiferroic thin film heterostructures. *Science* **299**, 1719–1722 (2003).

14. Wang, Y. *et al.* Magnetization switching by magnon-mediated spin torque through an antiferromagnetic insulator. *Science* **366**, 1125–1128 (2019).

15. Lebrun, R. *et al.* Tunable long-distance spin transport in a crystalline antiferromagnetic iron oxide. *Nature* **561**, 222–225 (2018).

16. Wang, H. *et al.* Spin-orbit-torque switching mediated by an antiferromagnetic insulator. *Phys. Rev. Appl.* **11**, 044070 (2019).

17. Chen, X. *et al.* Electric field control of Néel spin–orbit torque in an antiferromagnet. *Nature Mater.* **18**, 931–935 (2019).

18. Han, J. *et al.* Birefringence-like spin transport via linearly polarized antiferromagnetic magnons. *Nature Nanotechnol.* **15**, 563–568 (2020).

19. Dabrowski, M. *et al.* Coherent transfer of spin angular momentum by evanescent spin waves within antiferromagnetic nio. *Phys. Rev. Lett.* **124**, 217201 (2020).

20. Chen, X. *et al.* Observation of the antiferromagnetic spin Hall effect. *Nature Mater.* **20**, 800–804 (2021).

21. Zhang, P. *et al.* Control of néel vector with spin-orbit torques in an antiferromagnetic insulator with tilted easy plane. *Phys. Rev. Lett.* **129**, 017203 (2022).

22. Moon, J.-H. *et al.* Spin-wave propagation in the presence of interfacial Dzyaloshinskii-Moriya interaction. *Phys. Rev. B* **88**, 184404 (2013).

23. Iguchi, Y., Uemura, S., Ueno, K. & Onose, Y. Nonreciprocal magnon propagation in a noncentrosymmetric ferromagnet $LiFe_5O_8$. *Phys. Rev. B* **92**, 184419 (2015).

24. Gitgeatpong, G. *et al.* Nonreciprocal magnons and symmetry-breaking in the noncentrosymmetric antiferromagnet. *Phys. Rev. Lett.* **119**, 047201 (2017).

25. Tokura, Y. & Nagaosa, N. Nonreciprocal responses from non-centrosymmetric quantum materials. *Nat. commun.* **9**, 3740 (2018).

26. Kimura, T. *et al.* Magnetic control of ferroelectric polarization. *Nature* **426**, 55–58 (2003).

27. Chu, Y.-H. *et al.* Electric-field control of local ferromagnetism using a magnetoelectric multiferroic. *Nature Mater.* **7**, 478 (2008).

28. Zhao, T. *et al.* Electrical control of antiferromagnetic domains in multiferroic $BiFeO_3$ films at room temperature. *Nature Mater.* **5**, 823 (2006).

29. Rovillain, P. *et al.* Electric-field control of spin waves at room temperature in multiferroic $BiFeO_3$. *Nature Mater.* **9**, 975–979 (2010).

30. Gross, I. *et al.* Real-space imaging of non-collinear antiferromagnetic order with a single-spin magnetometer. *Nature* **549**, 252–256 (2017).

31. Sando, D. *et al.* Crafting the magnonic and spintronic response of $BiFeO_3$ films by epitaxial strain. *Nature Mater.* **12**, 641–646 (2013).

32. Fischer, P., Polomska, M., Sosnowska, I. & Szymanski, M. Temperature dependence of the crystal and magnetic structure of $BiFeO_3$. *J. Phys. C: Solid St. Phys.* **19**, 1931 (1980).

33. Haykal, A. *et al.* Antiferromagnetic textures in $BiFeO_3$ controlled by strain and electric field. *Nature Communs.* **11**, 1–7 (2020).

34. Ederer, C. & Spaldin, N. A. Weak ferromagnetism and magnetoelectric coupling in bismuth ferrite. *Phys. Rev. B* **71**, 060401(R) (2005).

35. Neaton, J. B., Ederer, C., Waghmare, U. V., Spaldin, N. A. & Rabe, K. M. First-principles study of spontaneous polarization in multiferroic $BiFeO_3$. *Phys. Rev. B* **71**, 014113 (2005).

36. Heron, J. *et al.* Deterministic switching of ferromagnetism at room temperature using an electric field. *Nature* **516**, 370–373 (2014).

37. Rahmedov, D., Wang, D., Íñiguez, J. & Bellaiche, L. Magnetic cycloid of $BiFeO_3$ from atomistic simulations. *Phys. Rev. Lett.* **109**, 037207 (2012).

38. Ramazanoglu, M. *et al.* Local weak ferromagnetism in single-crystalline ferroelectric $BiFeO_3$. *Phys. Rev. Lett.* **107**, 207206 (2011).

39. Yang, S. *et al.* Above-bandgap voltages from ferroelectric photovoltaic devices. *Nature Nanotechnol.* **5**, 143–147 (2010).

40. Zubko, P., Catalan, G. & Tagantsev, A. K. Flexoelectric effect in solids. *Annual Review of Materials Research* **43**, 387–421 (2013).

41. Huang, X. *et al.* Novel spin–orbit torque generation at room temperature in an all-oxide epitaxial $La_{0.7}Sr_{0.3}MnO_3/SrIrO_3$ system. *Adv. Mater.* **33**, 2008269 (2021).

42. Huang, Y.-L. *et al.* Manipulating magnetoelectric energy landscape in multiferroics. *Nature Commun.* **11**, 2836 (2020).

43. Manipatruni, S. *et al.* Scalable energy-efficient magnetoelectric spin–orbit logic. *Nature* **565**, 35–42 (2019).

44. Noël, P. *et al.* Non-volatile electric control of spin–charge conversion in a $SrTiO_3$ Rashba system. *Nature* **580**, 483–486 (2020).

45. Varotto, S. *et al.* Room-temperature ferroelectric switching of spin-to-charge conversion in germanium telluride. *Nature Electron.* **4**, 740–747 (2021).

46. Lesne, E. *et al.* Highly efficient and tunable spin-to-charge conversion through Rashba coupling at oxide interfaces. *Nature Mater.* **15**, 1261–1266 (2016).

47. Vaz, D. C. *et al.* Mapping spin–charge conversion to the band structure in a topological oxide two-dimensional electron gas. *Nature Mater.* **18**, 1187–1193 (2019).

48. Liu, L. *et al.* Spin-torque switching with the giant spin Hall effect of tantalum. *Science* **336**, 555–558 (2012).

49. Merbouche, H. *et al.* Voltage-controlled reconfigurable magnonic crystal at the sub-micrometer scale. *ACS Nano* **15**, 9775–9781 (2021).

50. Yi, D. *et al.* Tailoring magnetoelectric coupling in $BiFeO_3/La_{0.7}Sr_{0.3}MnO_3$ heterostructure through the interface engineering. *Adv. Mater.* **31**, 1806335 (2019).

51. Yu, P. *et al.* Interface control of bulk ferroelectric polarization. *PNAS* **109**, 9710–9715 (2012).

52. Parsonnet, E. *et al.* Non-volatile electric field control of thermal magnons in the absence of an applied magnetic field. *Phys. Rev. Lett.* **129**, 087601 (2022).

53. Wang, H. *et al.* Large spin-orbit torque observed in epitaxial $SrIrO_3$ thin films. *Appl. Phys. Lett.* **114**, 232406 (2019).

54. Cornelissen, L. J., Liu, J., Duine, R. A., Youssef, J. B. & Van Wees, B. J. Long-distance transport of magnon spin information in a magnetic insulator at room temperature. *Nature Phys.* **11**, 1022–1026 (2015).

55. Shikoh, E. *et al.* Spin-pump-induced spin transport in p-type Si at room temperature. *Phys. Rev. Lett.* **110**, 127201 (2013).

56. Nan, T. *et al.* Anisotropic spin-orbit torque generation in epitaxial $SrIrO_3$ by symmetry design. *PNAS* **116**, 16186–16191 (2019).

57. Mangeri, J. *et al.* Coupled magnetostructural continuum model for multiferroic $\mathrm{BiFeO_3}$. *Physical Review B* **108** (2023).

58. Cheng, R., Xiao, J., Niu, Q. & Brataas, A. Spin pumping and spin-transfer torques in antiferromagnets. *Phys. Rev. Lett.* **113** (2014).

59. Mangeri, J. *et al.* Topological phase transformations in ferroelectric nanoparticles. *Nanoscale* **9**, 1616–1624 (2017).

60. Permann, C. J. *et al.* Moose: Enabling massively parallel multiphysics simulation. *SoftwareX* **11**, 100430 (2020).

61. Liu, L., Moriyama, T., Ralph, D. C. & Buhrman, R. A. Spin-torque ferromagnetic resonance induced by the spin Hall effect. *Phys. Rev. Lett.* **106**, 036601 (2011).

62. Pai, C.-F., Ou, Y., Vilela-Leao, L. H., Ralph, D. C. & Buhrman, R. A. Dependence of the efficiency of spin Hall torque on the transparency of Pt/ferromagnetic layer interfaces. *Phys. Rev. B* **92**, 064426 (2015).

63. Wang, Y. *et al.* Topological surface states originated spin-orbit torques in $Bi_2\ Se_3$. *Phys. Rev. Lett.* **114**, 257202 (2015).

64. Rijnders, G., Blank, D. H., Choi, J. & Eom, C.-B. Enhanced surface diffusion through termination conversion during epitaxial $SrRuO_3$ growth. *Appl. Phys. Lett.* **84**, 505–507 (2004).

Methods

Sample and device fabrication

The tri-layers used in this study were grown by RHEED assisted pulsed laser deposition using a KrF laser with a wavelength of 248 nm. A 20 nm $La_{0.7}Sr_{0.3}MnO_3$ (5 nm $SrRuO_3$)layer was first grown at a substrate temperature 700°C and oxygen partial pressure 150 mTorr (100 mTorr), then a $BiFeO_3$ layer followed with various thicknesses at a substrate temperature 700°C and oxygen partial pressure 100 mTorr, and finally a 10 nm $SrIrO_3$ layer finished the growth at a substrate temperature 700°C and oxygen partial pressure 50 mTorr. The films were grown at a repetition of 2 (5 Hz) Hz, 10 Hz and 5 Hz with a laser fluence of 1.5 J/cm^2, 1.5 J/cm^2 and 1.2 J/cm^2, respectively. After the growth, the sample was cooled to room temperature in an oxygen environment of 750 Torr at a cooling rate of 10°C/min. To make ST-FMR devices, the samples were first spin coated with photoresist (MiR 701), then devices with a 50×25 μm^2 rectangular dimensions (15×10 μm^2 for the electric-field-controlled experiment) were made by photolithography (Heidelberg MLA 150) followed by ion milling (Pi scientific) that stopped at the $La_{0.7}Sr_{0.3}MnO_3$ layer. The remaining $La_{0.7}Sr_{0.3}MnO_3$ layer was used as the bottom electrode in the switching experiments; for the ST-FMR measurements this was patterned using a H_3PO_4 wet etch (H_3PO_4 : H_2O = 1 : 3). Finally, electrical contacts were made from 100 nm of Pt with a ground-signal-ground (GSG) geometry , so that when a GSG high-frequency probe made into contact with the samples the current traveling through the Pt contacts did not produce a net Oersted field at the sample.

Ferroelectric polarization switching

The ferroelectric polarizations was switched using a ferroelectric tester (Precision Multiferroic, Radiant Technologies), with a fixed frequency of $10kHz$ under room temperature. Two probes were placed on the SIO and FM layer respectively and two cycles of ferroelectric switching ($0 \rightarrow V_{max}$, $V_{max} \rightarrow -V_{max}$, $-V_{max} \rightarrow V_{max}$, $V_{max} \rightarrow -V_{max}$, $-V_{max} \rightarrow 0$) were carried out to make sure the ferroelectric polarization was fully switched. The final orientation of the ferroelectric polarization is determined by which electrode (top or bottom electrode) that the drive voltage from the tester is positioned on.

Antiferromagnetic spin wave calculations

To perform the spin wave calculations shown in Extended Fig. 16, we first use the phase field method to prepare a polar ground state corresponding to $\mathbf{P}||[111]$ and $\mathbf{P}||[\bar{1}\bar{1}\bar{1}]$ (along with an order parameter for the octahedral antiphase tilts). We then evolve a damped sublattice Landau-Lifshitz-Bloch equation to find the magnetic ground states corresponding to $\mathbf{L}||[\bar{1}01], \mathbf{m}||[1\bar{2}1]$ and $\mathbf{L}||[10\bar{1}], \mathbf{m}||[1\bar{2}\bar{1}]$ respectively. The simulation approach is outlined in Ref. [57]. This homogeneous noncollinear magnetic ground state without a cycloid texture is then perturbed with an applied sinc(x) field $\mathbf{H}||[\bar{1}01]$ with zero Gilbert damping ($\alpha = 0$), and the spin waves are set to propagate along $\pm\mathbf{k}||z$ in the linear limit. The detectable spin current in the AFM insulating layer[58] is proportional to $\mathbf{j} = \mathbf{j}^{\mathbf{l}} + \mathbf{j}^{\mathbf{m}} + \mathbf{j}^{\mathbf{ml}} + \mathbf{j}^{\mathbf{lm}}$ where $\mathbf{j}^{\mathbf{l}} \propto \mathbf{l} \times \dot{\mathbf{l}}$, $\mathbf{j}^{\mathbf{m}} \propto \mathbf{m} \times \dot{\mathbf{m}}$, $\mathbf{j}^{\mathbf{ml}} \propto \mathbf{m} \times \dot{\mathbf{l}}$, and $\mathbf{j}^{\mathbf{lm}} \propto \mathbf{l} \times \dot{\mathbf{m}}$. By time integrating the total spin current, the rectification (ratio) of *dc*-components is found to be $+0.978$. Calculations are performed using the Ferret module [59] which is part of the open-source MOOSE framework [60].

ST-FMR analysis

The ST-FMR signal, V_{mix}, is produced across the $La_{0.7}Sr_{0.3}MnO_3$/$BiFeO_3$/$SrIrO_3$ ST-FMR device as rectification of anisotropic magnetoresistance that oscillates at the same frequency as the input microwave current I_{RF}[61]. A microwave current at frequencies 4-6 GHz and power 12 dBm is applied to the device, with an in-plane external magnetic field oriented 45° with respect to the current direction. Finally, $V_{mix} = -\frac{1}{4}\frac{dR}{d\theta}\frac{\gamma I_{RF} cos\theta}{2\pi\Delta(df/dH)_{H_{ext}=H_0}}(\tau_{DL}F_S(H_{ext}) + \tau_{FL}F_A(H_{ext}))$[61], where $dR/d\theta$ is the angle dependent magnetoresistance at θ, γ is the gyromagnetic ratio, Δ is the linewidth of the ST-FMR signal, $(df/dH)_{H_{ext}=H_0}$ is the field gradient of the resonance frequency, τ_{DL} is the damping-like torque, τ_{FL} is the field-like torque, $F_S(H_{ext})$ is the symmetric Lorentzian function and $F_A(H_{ext})$ is the anti-symmetric Lorentzian function respectively, is detected by Keithley 2182A nanovoltmeter, from the fits of which the symmetric component V_S and the anti-symmetric component V_A, which are associated with damping-like torque (τ_{DL}) and field-like torque (τ_{FL}) respectively, can be extracted. As a result, spin orbit torque efficiency-ξ_{SOT} is evaluated using $\xi_{DL} = \frac{2e\tau_{DL}m_s t_{FM}}{J_c\hbar}$, where $\tau_{DL} = \frac{4V_s\Delta}{I_{RF}cos\theta\frac{dR}{d\theta}}\frac{1+\frac{\mu_0 M_{eff}}{2B_{res}}}{(\frac{1+\mu_0 M_{eff}}{B_{res}})^{1/2}}$[62,63]. The SOT efficiency for the samples in this work was measured from 4 GHz to 6 GHz and the error bar in Fig. 2 is a result of SOT efficiencies across different frequencies, while the error bar in extended Fig. 6 is caused by the SOT efficiency distribution across different devices.

Data availability

The data that support the findings of this study are available from the corresponding authors on reasonable request.

Acknowledgements

We are grateful for the fruitful discussions with Prof. Albert Fert, Dr. Eric Parsonnet, Dr. Yenlin Huang. X.H., D.C.R. and R.R. acknowledge the support from the SRC-JUMP ASCENT center. R.J. acknowledges the support from the U.S. Department of Energy, under contract No. DE-SC0017671. X.C., P.S., D.V., S.S., L.W.M., Z.Y., and R.R. acknowledge partial support from the U.S. Department of Energy, Office of Science, Office of Basic Energy Sciences, Materials Sciences and Engineering Division under Contract No. DE-AC02-05-CH11231 (Codesign of Ultra-Low-Voltage Beyond CMOS Microelectronics for the development of materials for low-power microelectronics). Y.L. and R.C. acknowledge the support from the Air Force Office of Scientific Research under Grant No. FA9550-19-1-0307. T.W. and Z.Q.acknowledge the support from US Department of Energy, Office of Science, Office of Basic Energy Sciences, Materials Sciences and Engineering Division under Contract No. DE-AC02-05CH11231 (van der Waals heterostructures program, KCWF16). This research used resources of the Advanced Light Source, which is a DOE Office of Science User Facility under contract no. DE-AC02-05CH11231. H.P. acknowl-

edges support from Army Research Office and Army Research Laboratory via the Collaborative for Hierarchical Agile and Responsive Materials (CHARM) under cooperative agreement W911NF-19-2-0119. J.M. has received funding from the European Union's Horizon 2020 research and innovation programme under the Marie Skłodowska-Curie grant agreement SCALES - 897614. D.R.R. acknowledges funding from the Ministerio dell'Università e della Ricerca, Decreto Ministeriale n. 1062 del 10/08/2021 (PON Ricerca e Innovazione). O.H. acknowledges support from the US Department of Energy, Office of Science, Basic Energy Sciences, Division of Materials Sciences and Engineering.

Author contributions

X.C. and R.R. supervised this study. X.H. carried out the synthesis and characterization of heterostructures. X.H. and X.C. fabricated the devices. X.H. and R.J. carried out the ST-FMR measurements. X.H. and X.C. carried out the current induced magnetization switching measurements. C.X., H.T. performed the non-local transport measurements. C.K. performed dynamic XMCD measurements at beamline 4.0.2 of the Advanced Light Source. Y.L. and R.C performed the theoretical calculations. J.M., D.R.R. O.H., and J.I. developed and performed the coupled polar-micromagnetic simulations. X.C., D.V., and Z.Y. devised the electronic model and performed the calculations. S.S. performed the microstructure and electronic structure characterizations. H.Z., T.W., L.C., C.H., I.H., S.H., H.P., J.Y., P.M., P.S., Z.Q., S.S., M.R., D.S., L.W.M., D.C.R., and A.F. gave suggestions on the experiments. All authors discussed the results and prepared the manuscript.

Competing interests

The authors declare no competing interests.

Additional information

Correspondence and requests for materials should be addressed to X.C. and R.R. Reprints and permissions information is available at http://www.nature.com/reprints.

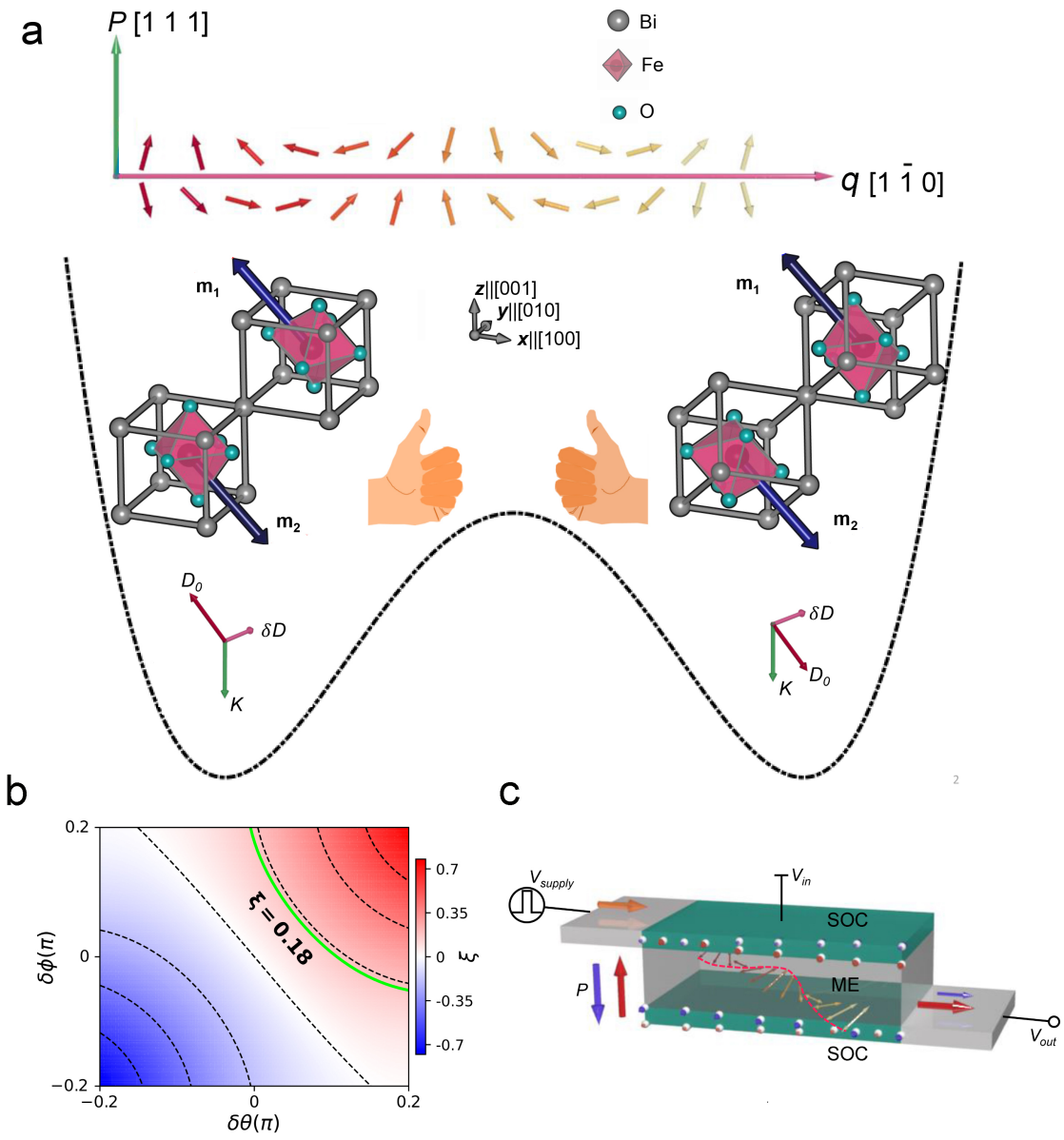


Figure 1: Concept of chiral magnon transport in multiferroics. a, A sketch of spin cycloid that propagates along $\boldsymbol{q} = [1\bar{1}0]$. $\boldsymbol{P}$ is the ferroelectric polarization pointing along $[111]$, $\boldsymbol{D}_0$ (along $[\bar{1}\bar{1}2]$) is the intrinsic DMI vector responsible for the spin cycloid formation, and $\delta\boldsymbol{D}$ is the extrinsic DMI vector induced by the built-in electric field in $BiFeO_3$. The double well is a schematic of the bi-stable states of ferroelectric polarization. Upon the reversal of $\boldsymbol{P}$, $\boldsymbol{D}_0$ switches by $180°$ while $\delta\boldsymbol{D}$ remains unchanged, flipping the sign of the hybrid product $(\boldsymbol{D}_0 \times \delta\boldsymbol{D}) \cdot \boldsymbol{K}$ with $\boldsymbol{K}$ the magnon wave vector, hence a chirality flip of the three vectors. **b,** Rectification ratio of spin current [defined by Eq. (1)] as a function of $\delta\theta$ and $\delta\phi$, which are the spherical angles of $\delta\boldsymbol{D}$ relative to the direction of $\boldsymbol{D}_0$. The solid line marks the experimental value $\xi = 0.18$. **c,** Buffer logic consists of spin injection in the top SOC layer (dark green), magnetoelectric control of spin transmission in the intermediate ME layer (translucent), and spin detection in the bottom SOC layer (dark green). The switching of the polar order is controlled by $\boldsymbol{V}_{in}$. $\boldsymbol{V}_{supply}$ serves as the source for spin Hall current injection. The small (purple) and large (red) output voltages $\boldsymbol{V}_{out}$ in **c** correspond to spin transport of downward and upward ferroelectric polarization in **a** respectively.

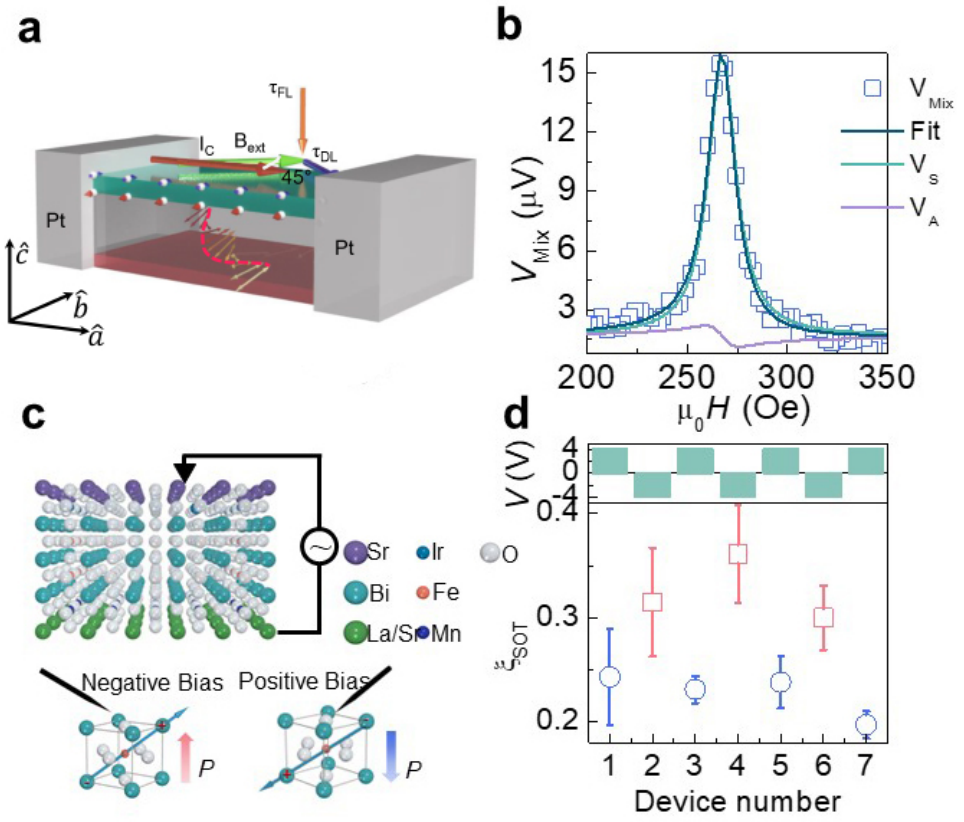


Figure 2: Spin transmission controlled by ferroelectric polarization in $BiFeO_3$. **a,** A 3D schematic illustration for the ST-FMR measurement. Top : $SrIrO_3$, middle : $BiFeO_3$, bottom : $La_{0.7}Sr_{0.3}MnO_3$. $\boldsymbol{I}_c$ represents the radio frequency microwave current, which flows at a $45°$ angle with respect to the in-plane external magnetic field represented by $\boldsymbol{B}_{ext}$. A spin cycloid that lies in $(\bar{1}\bar{1}2)$ plane, and propagates along $[1\bar{1}0]$ direction is dipicted by the double-headed arrows. **b,** Measured ST-FMR signal at room temperature for 12 dBm of applied microwave power at 4 GHz for a sample $La_{0.7}Sr_{0.3}MnO_3$ (20 nm)/$BiFeO_3$ (25 nm)/$SrIrO_3$ (10 nm) of dimension 5×15 μm^2. The lines are Lorentzian fits to the mixing voltage as described in methods (ST-FMR analysis section), showing both symmetric and anti-symmetric components. **c,** A schematic of a $La_{0.7}Sr_{0.3}MnO_3$ (20 nm) /$BiFeO_3$ (25 nm) /$SrIrO_3$ (10 nm) heterostructure subject to an external electric field, along with schematics of the $BiFeO_3$ ferroelectric polarization under negative and positive biases. **d,** The SOT efficiency measured with the ST-FMR technique as a function of bias voltages applied beforehand for samples of $La_{0.7}Sr_{0.3}MnO_3$ (20 nm) /$BiFeO_3$ (25 nm) /$SrIrO_3$ (10 nm). The open squares (circles) represent the SOT efficiency for the tri-layer with negative (positive) bias voltages applied on the top electrode - $SrIrO_3$.

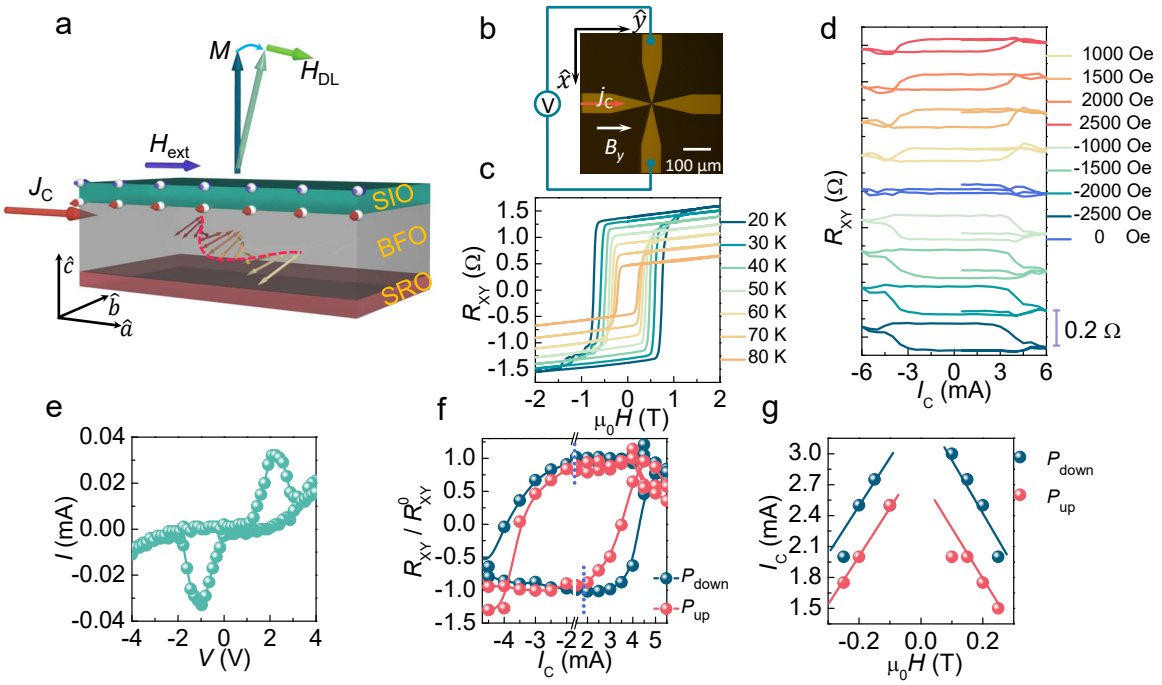


Figure 3: Magnetization switching induced by the spin torque in $BiFeO_3$ under the control of ferroelectric polarization. a, A schematic demonstrating the magnetization switching of $SrRuO_3$ by the current-induced torques borne by the magnons transmitted through $BiFeO_3$ for a sample $SrRuO_3$ (5 nm)/$BiFeO_3$ (25 nm)/$SrIrO_3$ (10 nm). A spin cycloid that lies in $(\bar{1}\bar{1}2)$ plane, and propagates along $[1\bar{1}0]$ direction is depicted by the double-headed arrows. The torque carried by the transmitted magnons switches the magnetic moment (dark blue arrows) of the neighboring $SrRuO_3$ layer in the out-of-plane direction. A small assisting magnetic field ($\boldsymbol{H}_{ext}$) is applied along the pulsed current ($\boldsymbol{J}_C$) direction. **b,** An optical image of the actual Hall device used in the anomalous Hall effect (AHE) and magnetization switching measurements. **c,** Anomalous Hall resistance ($\boldsymbol{R}_{XY}$) as a function of the magnetic field at various temperatures for the heterostructure $SrRuO_3$ (5 nm)/$BiFeO_3$ (25 nm)/$SrIrO_3$ (10 nm) is shown on the bottom. A dc current of 100 μA is applied during the AHE measurements. **d,** R_{XY} as a function of pulsed currents at $70K$. External magnetic fields with different polarities and strengths are applied along the current pulse direction to assist the magnetization switching. After each current pulse, a dc current of 100 μA is applied to detect the change in $\boldsymbol{R}_{XY}$. The hysteretic magnetization switching loops are shifted with respect to the magnetization switching loop at zero assisting field for display. The current pulses have a pulse width of 1 ms. **e,** An example IV curve collected during the ferroelectric switching experiments for the heterostructure $SrRuO_3$ (5 nm)/$BiFeO_3$ (25 nm)/$SrIrO_3$ (10 nm). **f,** An example ferroelectric polarization controlled magnetization switching measurement. The magnetization switching behavior for $SrRuO_3$ (5 nm)/$BiFeO_3$ (25 nm)/$SrIrO_3$ (10 nm) heterostructure with the polarization of $BiFeO_3$ pointing from the bottom (top) electrode to the top (bottom) electrode is shown in red (blue). The $\boldsymbol{R}_{XY}$ is normalized for better display. **g,** The magnitudes of critical switching current as a function of the applied external magnetic fields are summarized. The critical switching current for $SrRuO_3$ (5 nm)/$BiFeO_3$ (25 nm)/$SrIrO_3$ (10 nm) heterostructure with upward (downward) ferroelectric polarization is shown in red (blue). The lines are a guide to the eye.

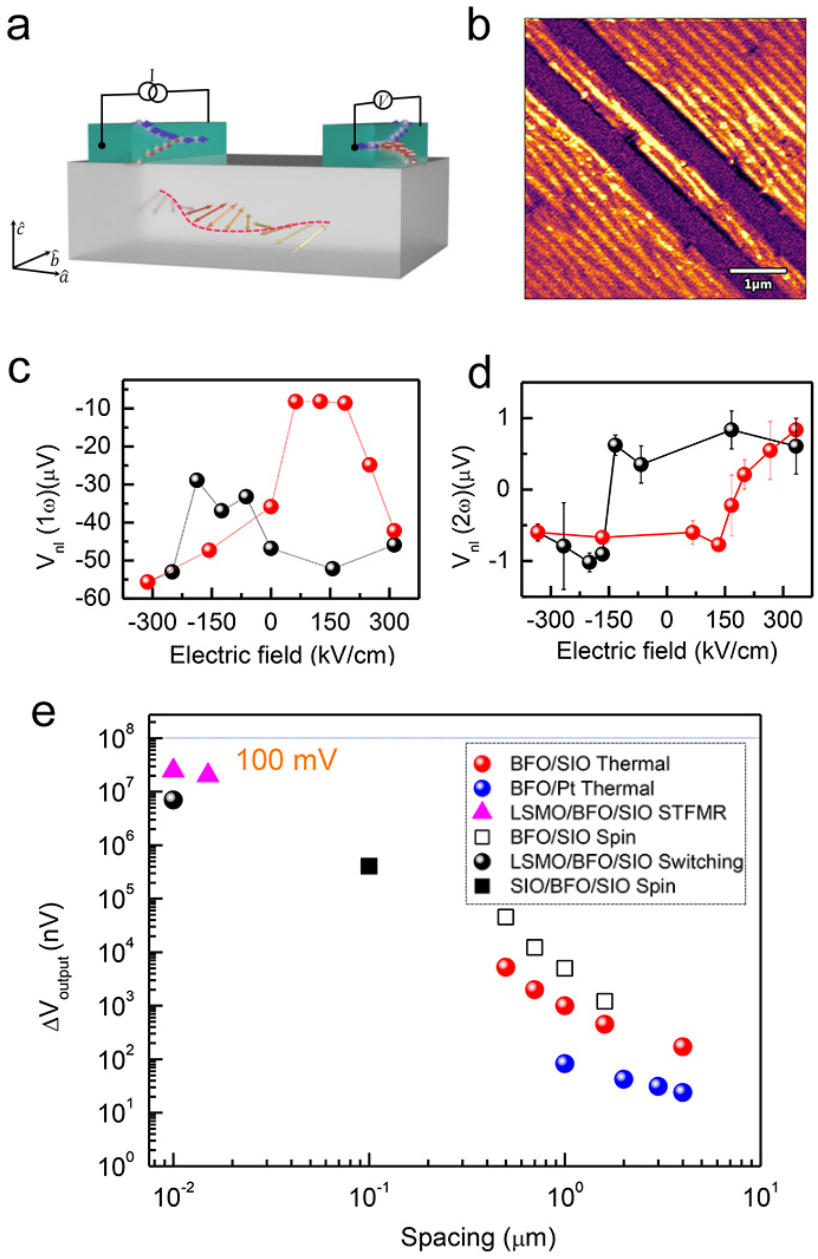
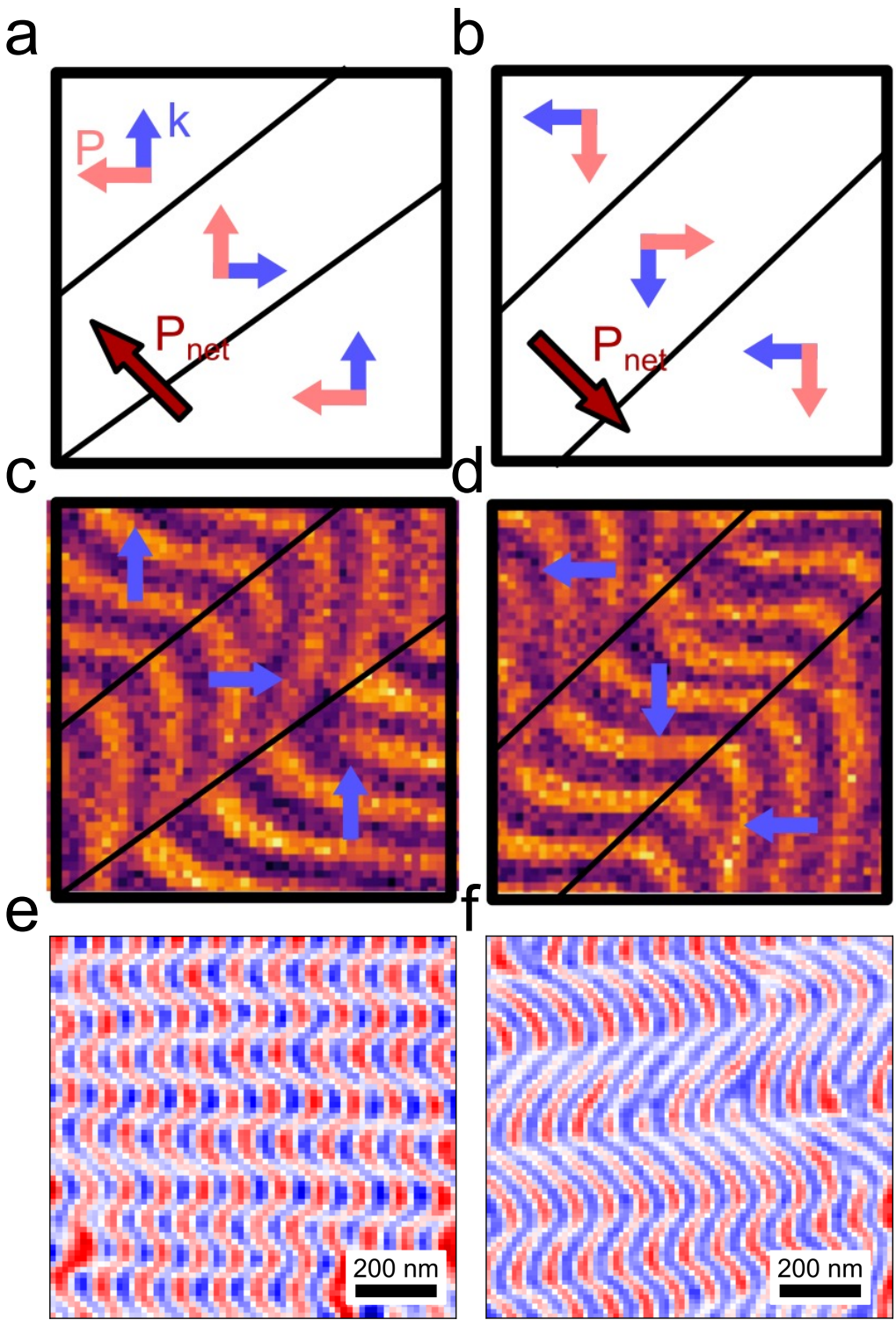
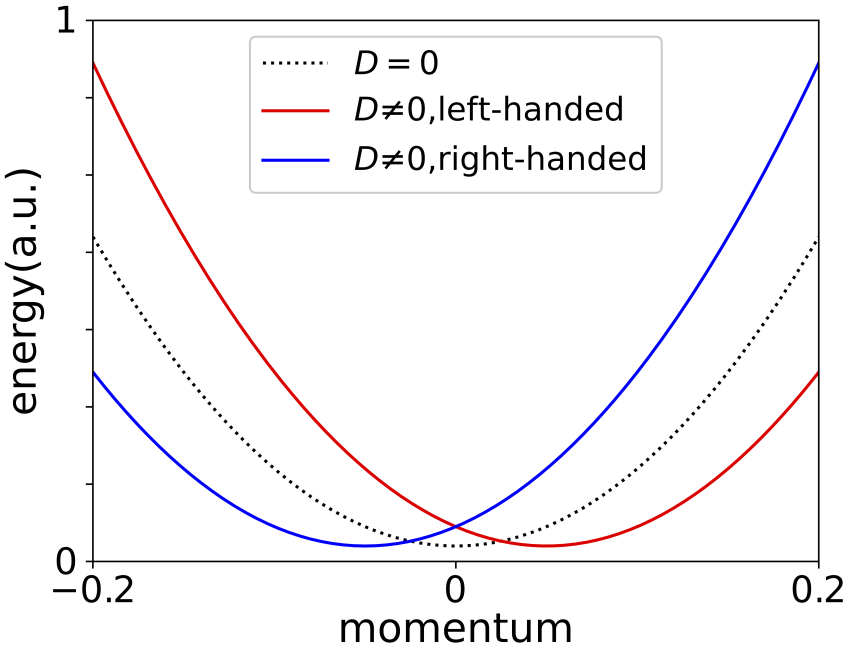


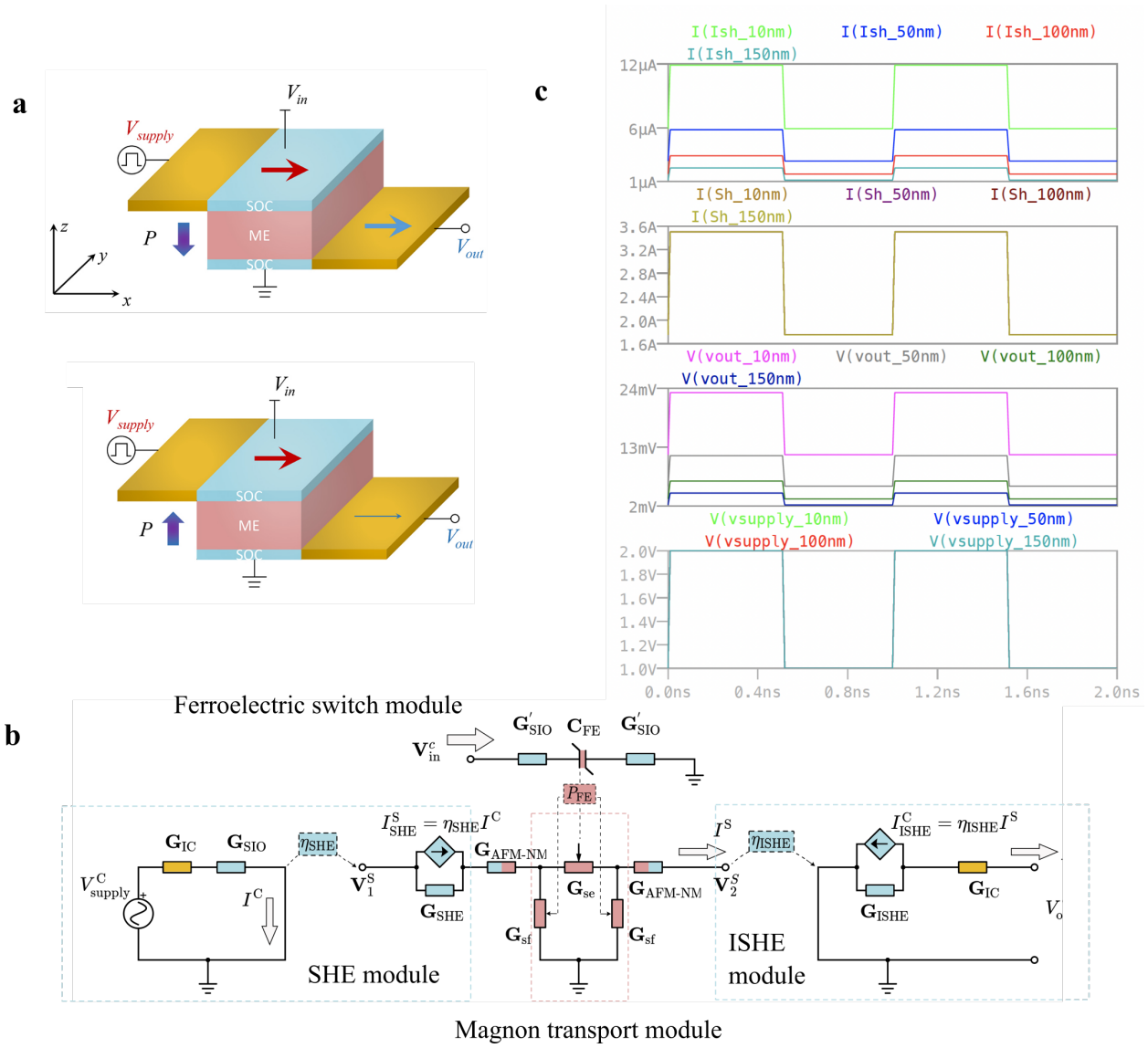
Figure 4: Magnetoelectric spin-orbit logic based on controllable magnon transport in $BiFeO_3$. a, Schematic of the non-local device formed with a magnetoelectric test structure. **b,** Piezo-force microscopy image of the non-local device structure. The channel width is 0.5 μm. **c,** Hysteresis loop from spin magnon readout in $SrIrO_3$ with first harmonic measurements for a device with a 500 nm channel width. **d,** Hysteresis loop from thermal magnon readout in $SrIrO_3$ with second harmonic measurements in a device with a 1 μm channel width. **e,** Output voltage scaling with channel spacing for measurements in nonlocal devices (points for spacings 0.5 μm and above), vertical structure of SIO/BFO/SIO when BFO is 100 nm, and estimates of voltages that could be obtained for vertical transport of magnons through 10 and 15 nm of $BiFeO_3$. The power is fixed at 3 mW.



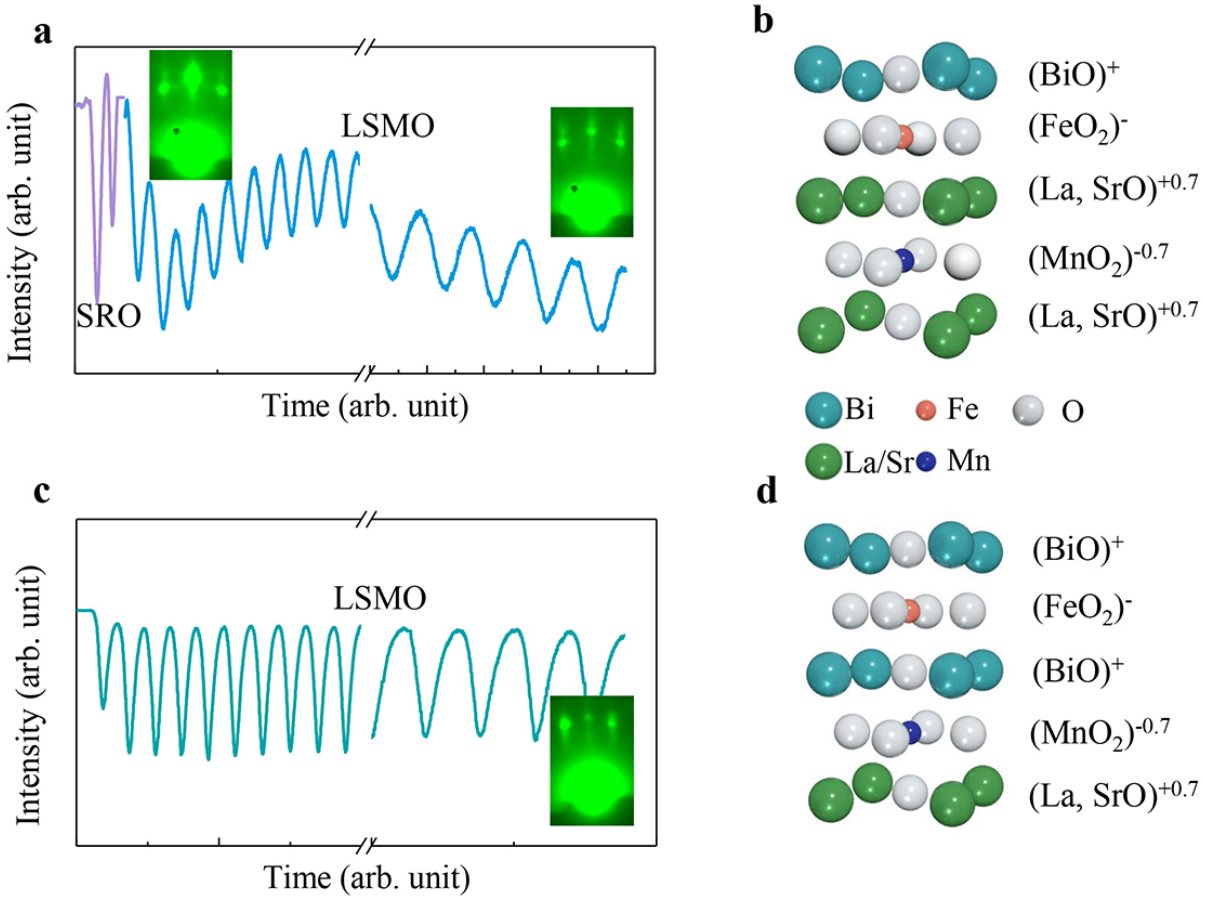
Extended Data Fig. 1. NV magnetometry image for $BiFeO_3$. a, c, Schematic illustrations of ferroelectric domains and the corresponding spin cycloid propagation directions before and after polarization switching. The pink arrows represent the ferroelectric polarization orientations.**b, d,** Magnetic stray field distribution recorded with scanning NV magnetometer for 100 nm $BiFeO_3$ before and after polarization switching. The blue arrows are the spin cycloid propagation wave vector.**e, f,** Magnetic stray field distribution recorded with scanning NV magnetometer for 30 nm and 100 nm $BiFeO_3$ respectively.



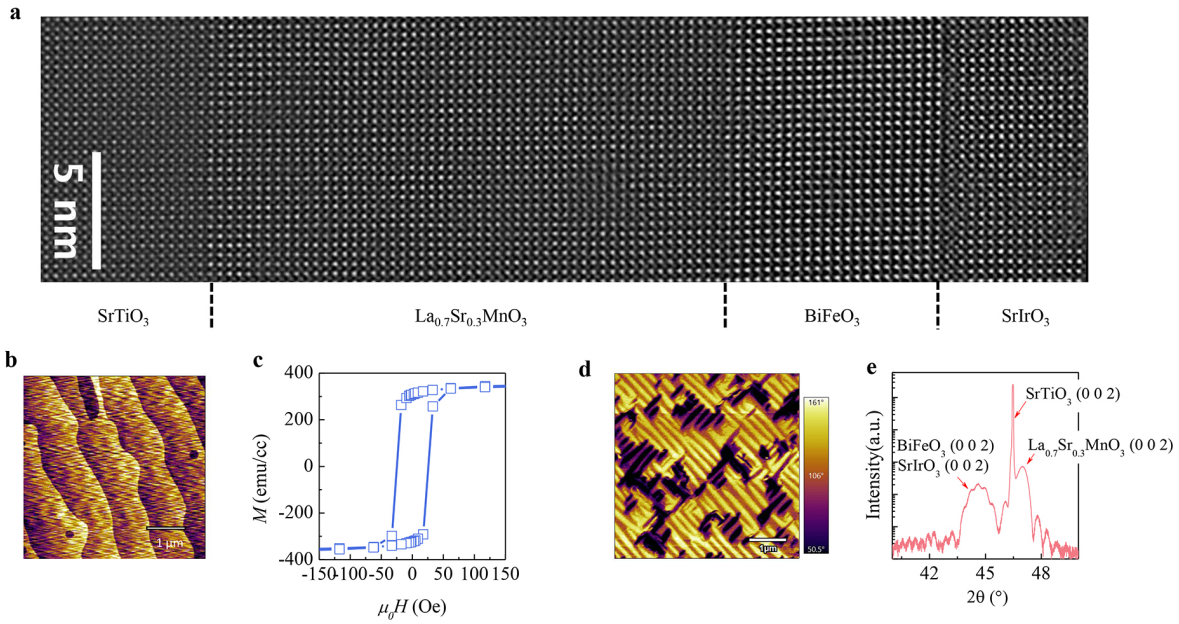
Extended Data Fig. 2. Schematic magnon band for $BiFeO_3$ Schematic magnon band dispersion for $BiFeO_3$ in the absence (D=0) and presence (D0) of the Dzyaloshinskii-Moriya interaction. In the absence of the Dzyaloshinskii-Moriya interaction (D=0), magnon bands are doubly degenerate due to the combined PT-symmetry (black dashed line). These degenerate magnon bands are linearly-polarized. Introducing Dzyaloshinskii-Moriya interaction breaks the degeneracy, resulting in two shifted circularly polarized magnon bands (colorful lines).



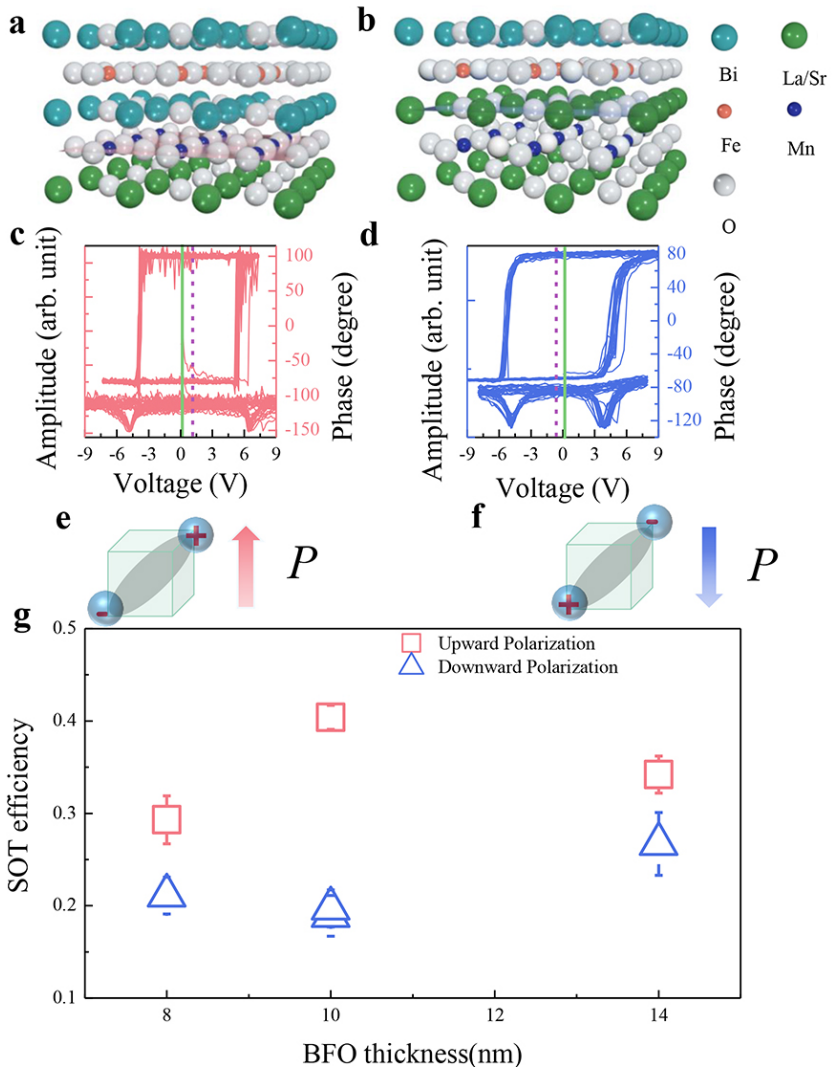
Extended Data Fig. 3. Schematics for magnon-mediated MESO logic device. **a,** Same schematics duplicated from Fig. 1d. **b,** Modularized circuit schematics. The top module is the ferroelectric switch module, where the input voltage $V_{\rm in}^{c}$ switches the direction of the ferroelectric polarization $P_{\rm FE}$ in the magnetoelectric layer. Such polarization change also affects the spin conductance $G_{\rm se}$ and $G_{\rm sf}$ of the ME layer. The leftmost and rightmost modules represent the spin Hall effect (SHE) process in the top SOC layer (injector) and the inverse spin Hall effect (ISHE) process in the bottom SOC layer (detector), respectively. The current-controlled spin current source $I_{\rm SHE}^{S}$ in the SHE module depends on the output charge current of the top SOC layer. Similarly, the current-controlled charge current source $I_{\rm ISHE}^{C}$ in the ISHE module depends on the output spin current of the bottom SOC layer. The parameters $\eta_{\rm SHE}$ and $\eta_{\rm ISHE}$ represent the charge-to-spin and spin-to-charge current conversion rates, respectively. The module in the middle describes the magnon transport process in the ME layer, which is connected to the SHE and ISHE modules through the spin conductance at the interfaces between ME and SOC layers, denoted as $G_{\rm AFM-NM}$. **c,** Lossy Buffer logic simulation result for the equivalent circuit in Fig. 3b where the output follows the input pulse signal characteristics.



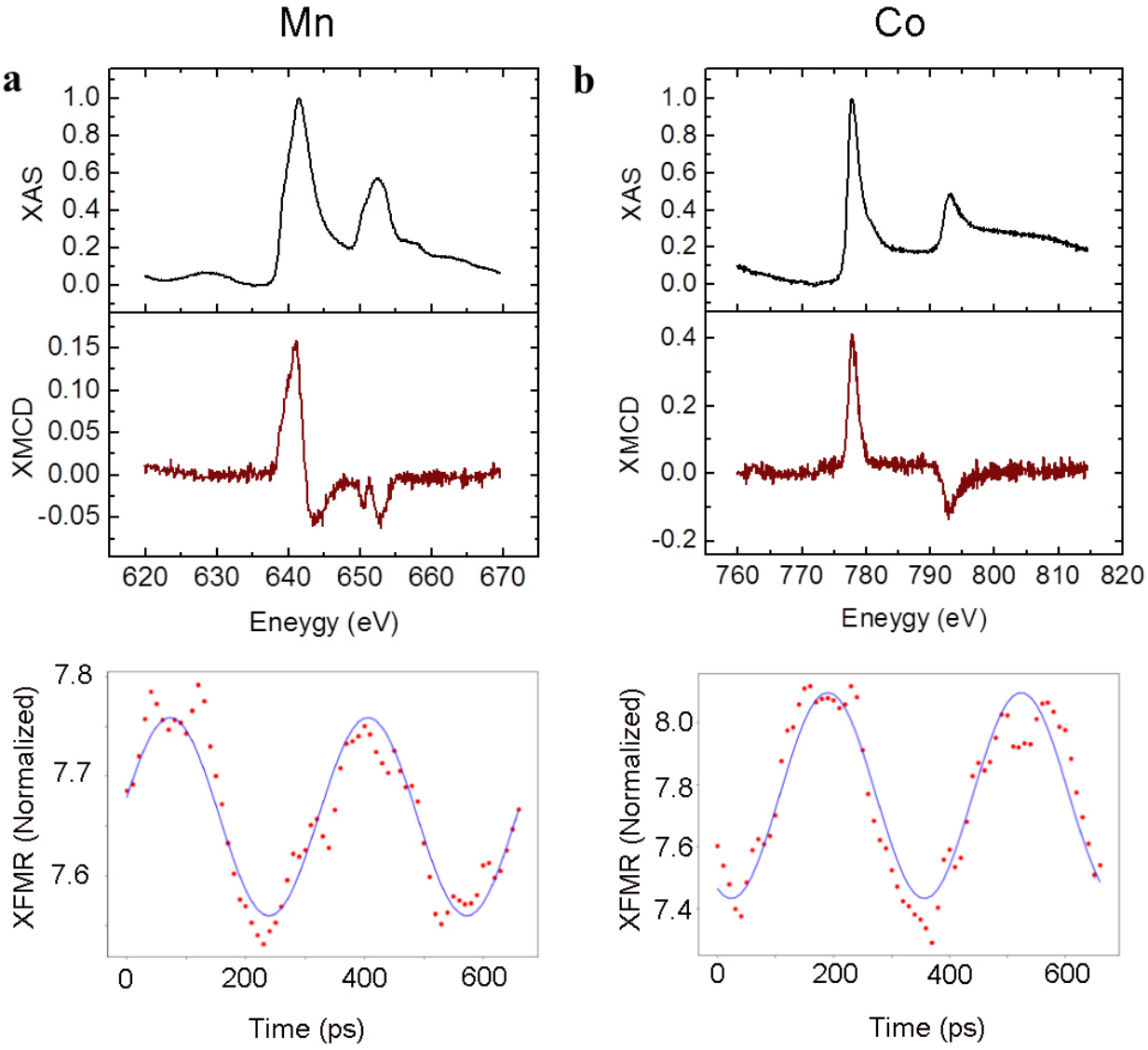
Extended Data Fig. 4. Atomic scale control of interface termination by pulsed laser deposition. a, RHEED intensity oscillation of the specularly reflected beam during the growth of $SrRuO_3$ and $La_{0.7}Sr_{0.3}MnO_3$ on TiO_2-terminated $SrTiO_3$ [001] surface. A growth of 2.5 unit-cell of $SrRuO_3$ on TiO_2 terminated $SrTiO_3$ substrate is required in order to achieve the SrO terminated substrate, due to the fact that RuO is highly volatile at high temperatures and $SrRuo_3$ is therefore self-terminated with SrO layer[64].**b,** A schematic of the resulting $La_{0.7}Sr_{0.3}O$-FeO_2 interface. **c,** RHEED intensity oscillation of the specular beam during the growth of $La_{0.7}Sr_{0.3}MnO_3$ by direct on TiO_2-terminated $SrTiO_3$ [001] surface. **d,** A schematic of the resulting MnO_2-BiO interface.



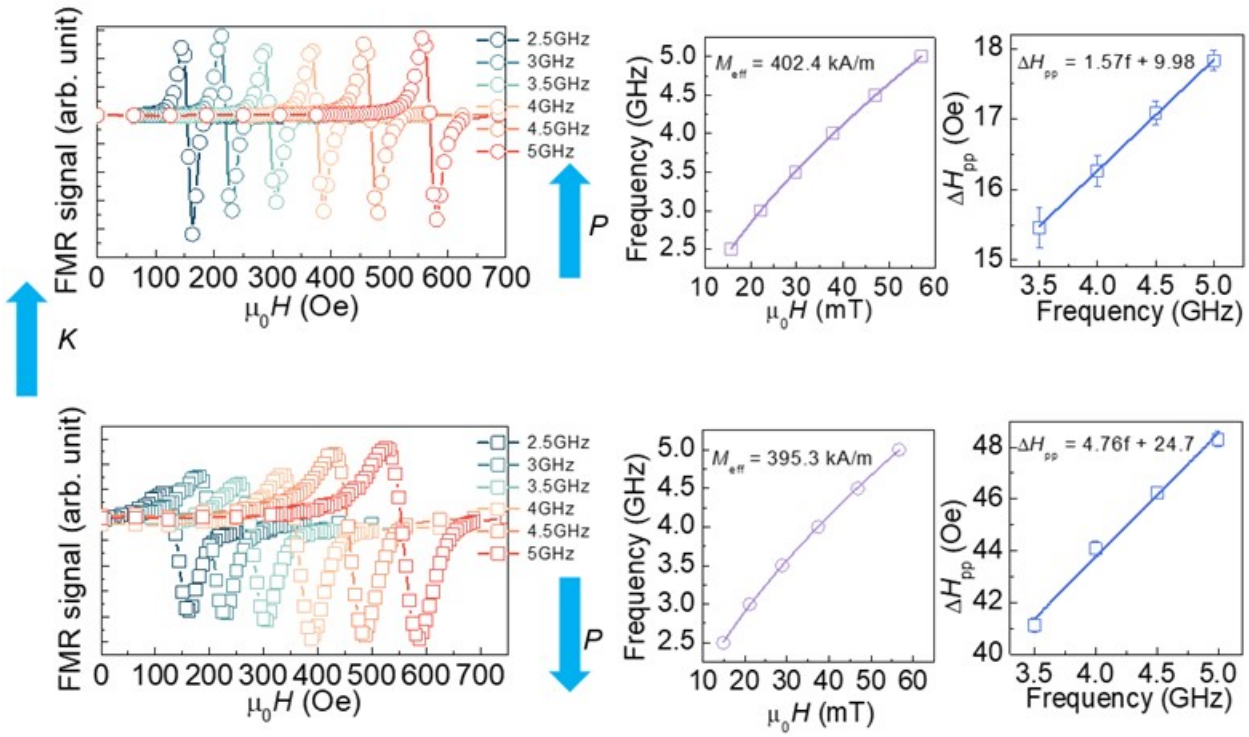
Extended Data Fig. 5. Structure, magnetization, ferroelectric domain structure measurements for $La_{0.7}Sr_{0.3}MnO_3/BiFeO_3/SrIrO_3$ heterostructure. **a,** HAADF image of $La_{0.7}Sr_{0.3}MnO_3/BiFeO_3/SrIrO_3$ tri-layer, displaying atomically sharp interfaces and high crystal quality. **b,** HF etched and thermally annealed $SrTiO_3$ substrate with atomic steps and terraces. **c,** Magnetization vs applied magnetic field (MH) measurement for $La_{0.7}Sr_{0.3}MnO_3/BiFeO_3/SrIrO_3$, showing a coercivity of ~ 25 Oe and a saturation magnetization ~ 320 emu/cc. **d,** In-plane piezoresponse microscopy (PFM) image of the $BiFeO_3$ layer. **e,** High resolution XRD 2θ-ω scan of the tri-layer



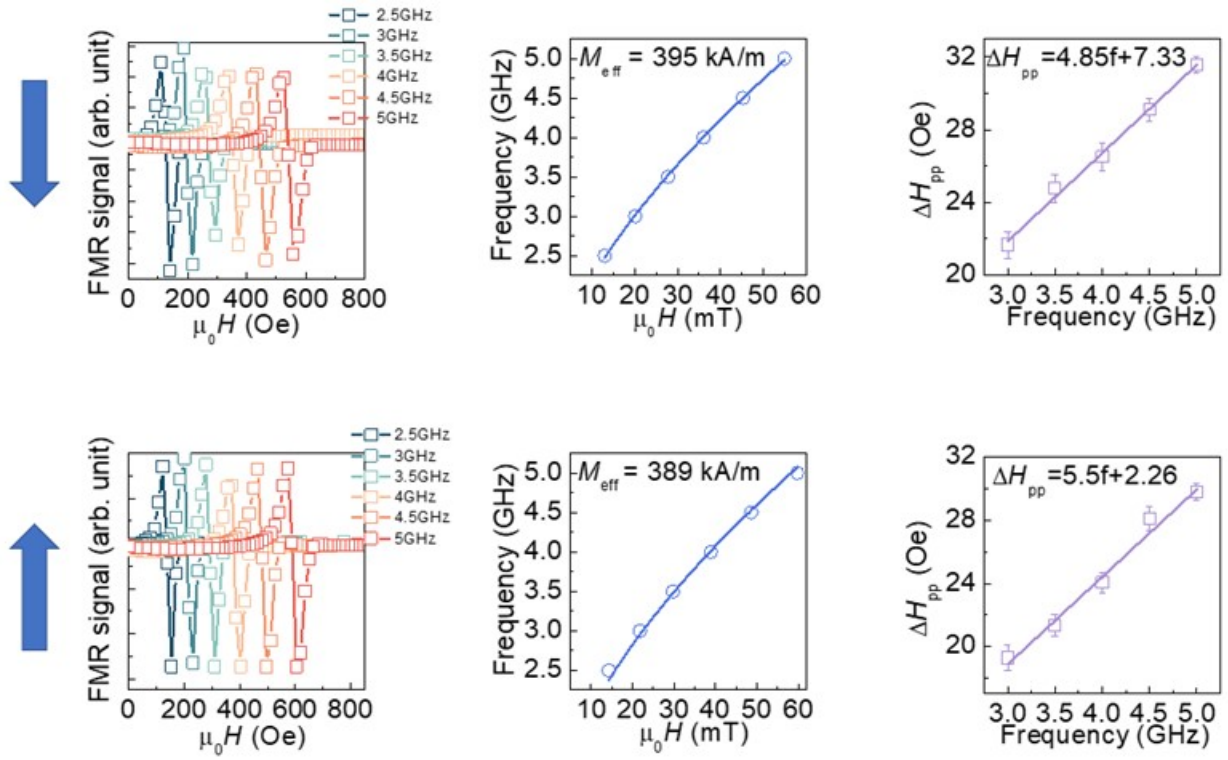
Extended Data Fig. 6. Ferroelectric control of spin transport enabled by the interface chemistry. a, A schematic for $La_{0.7}Sr_{0.3}MnO_3/BiFeO_3$ atomic stacking, where $La_{0.7}Sr_{0.3}O$-MnO_2-BiO-FeO_2 is stacked at the interface. **b,** A schematic for $La_{0.7}Sr_{0.3}MnO_3/BiFeO_3$ atomic stacking, where MnO_2-$La_{0.7}Sr_{0.3}O$-FeO_2-BiO is stacked at the interface. **c,** Corresponding piezoresponse for $La_{0.7}Sr_{0.3}O$-MnO_2-BiO-FeO_2 stacking ($La_{0.7}Sr_{0.3}MnO_3$(12 nm)/$BiFeO_3$(50 nm)), with top and bottom being phase and amplitude respectively. The solid line denotes the shifting of the piezoresponse curves to zero volts, indicating an upward ferroelectric polarization for $La_{0.7}Sr_{0.3}O$-MnO_2-BiO-FeO_2 stacking. **d,** Corresponding piezoresponse for MnO_2-$La_{0.7}Sr_{0.3}O$-FeO_2-BiO stacking ($La_{0.7}Sr_{0.3}MnO_3$(12 nm)/$BiFeO_3$(50 nm)), with the top and bottom being phase and amplitude respectively. The solid line denotes the shifting of the piezoresponse curves to zero volts, indicating a downward ferroelectric polarization for MnO_2-$La_{0.7}Sr_{0.3}O$-FeO_2-BiO stacking. **e,f,** An artistic illustration for upward and downward ferroelectric polarization. **g,** Spin orbit torque efficiency for $BiFeO_3$ with different polarization states as a function of $BiFeO_3$ thicknesses. The red (blue) data points represent the spin-orbit torque efficiency for $La_{0.7}Sr_{0.3}MnO_3/BiFeO_3/SrIrO_3$, where $BiFeO_3$ has an upward (downward) polarization.



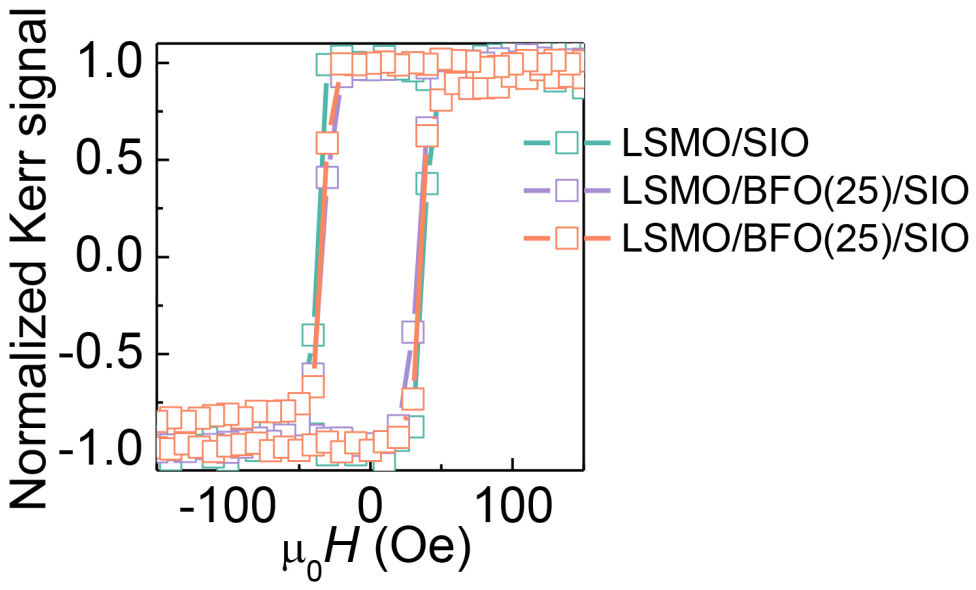
Extended Data Fig. 7. X-ray magnetic circular dichroism spectra for the X-ray Ferromagnetic resonance measurements in LSMO/BFO/Ti/CoFe Stacks. a, b, X-ray absorption spectra (XAS), X-ray magnetic circular dichroism spectra (XMCD), and X-ray ferromagnetic resonance (XFMR) of Mn(a) and Co(b), which correspond to the magnetic element in LSMO and CoFe respectively. The X-FMR measurements confirm the ac spin current transport through BFO.



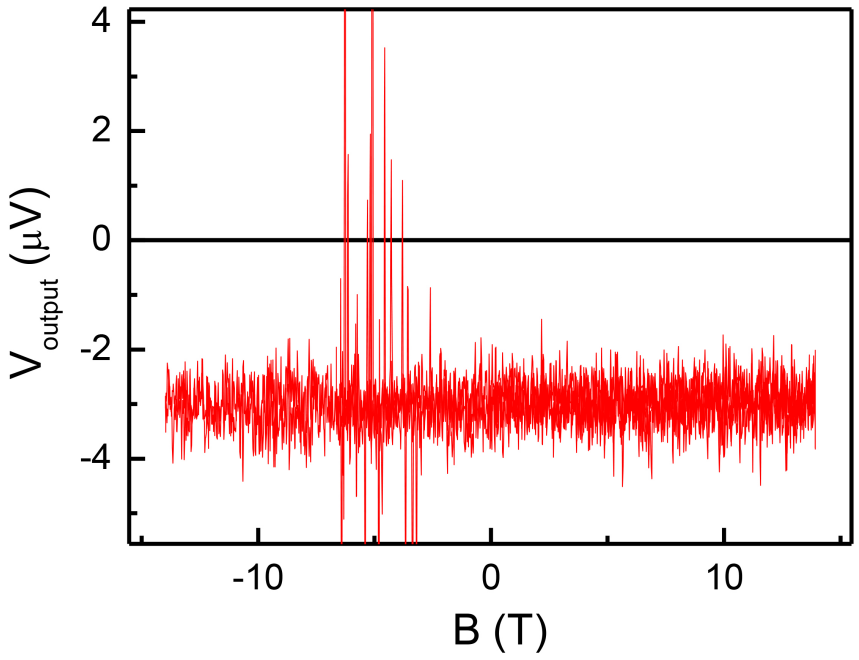
Extended Data Fig. 8. FMR measurements for LSMO (20 nm)/BFO (10 nm)/SIO (10 nm) samples with different polarizations. a, b, FMR spectrum for LSMO/BFO/SIO heterostructures with upward and downward ferroelectric polarizations respectively. Arrow K is a representation of spin propagation with respect to the polarization direction for FMR measurements. Resonance fields and frequencies are summarized in **c** and **d** for heterostructures with upward and downward respectively. Effective magnetization 402 kA/m and 395 kA/m are determined with Kittel equation fitting. **e, f,** Peak-to-peak linewidth as a function of frequency is shown for heterostructures with upward and downward polarizations respectively. Effective Gilbert damping constants (α) of 0.00381 and 0.0116 are estimated for systems with upward and downward polarizations respectively



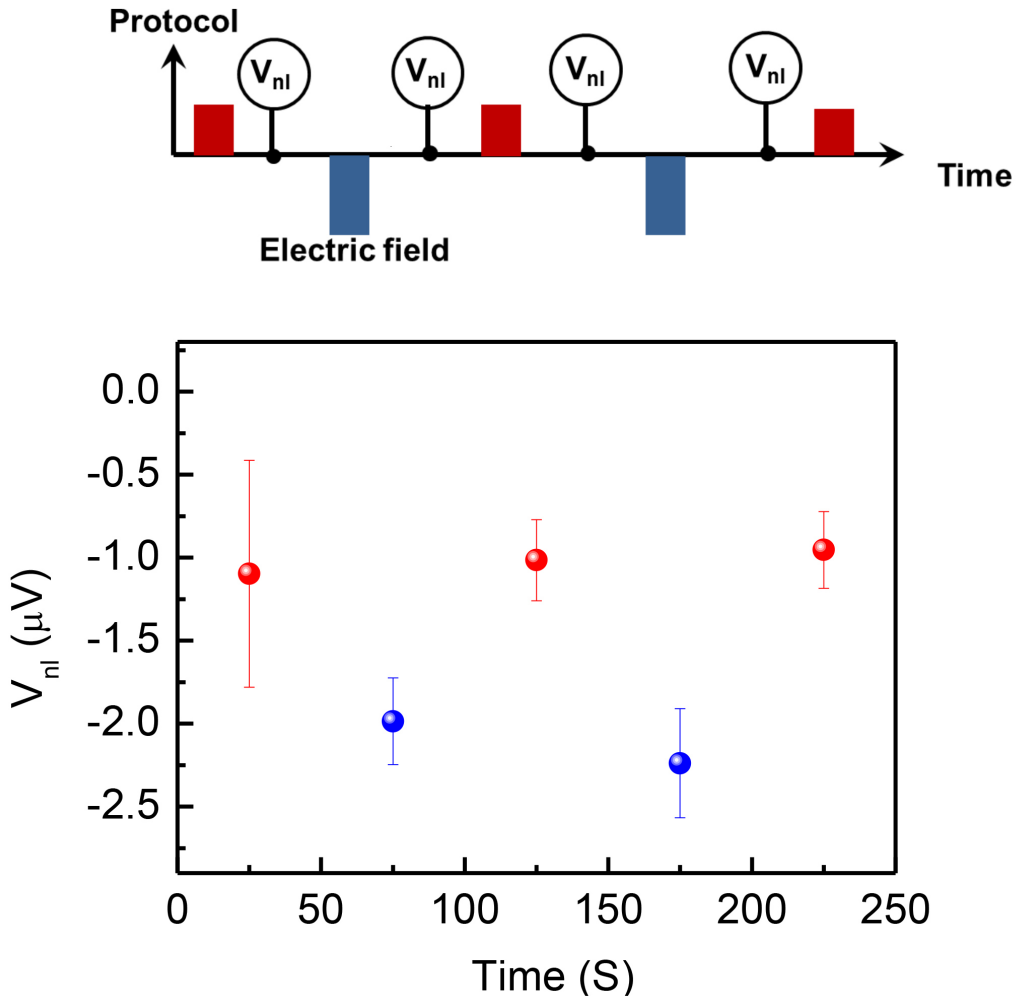
Extended Data Fig. 9. FMR measurements for LSMO (20 nm)/BFO (40 nm) samples with different polarizations. a, b, FMR spectrum for LSMO/BFO heterostructures with downward and upward ferroelectric polarizations respectively. Resonance fields and frequencies are summarized in **c** and **d** for heterostructures with downward and upward respectively. Effective magnetization 395 kA/m and 389 kA/m are determined with Kittel equation fitting. **e, f,** Peak-to-peak linewidth as a function of frequency is shown for heterostructures with downward and upward polarizations respectively. Effective Gilbert damping constants of 0.01177 and 0.013335 are deduced for downward and upward polarizations respectively



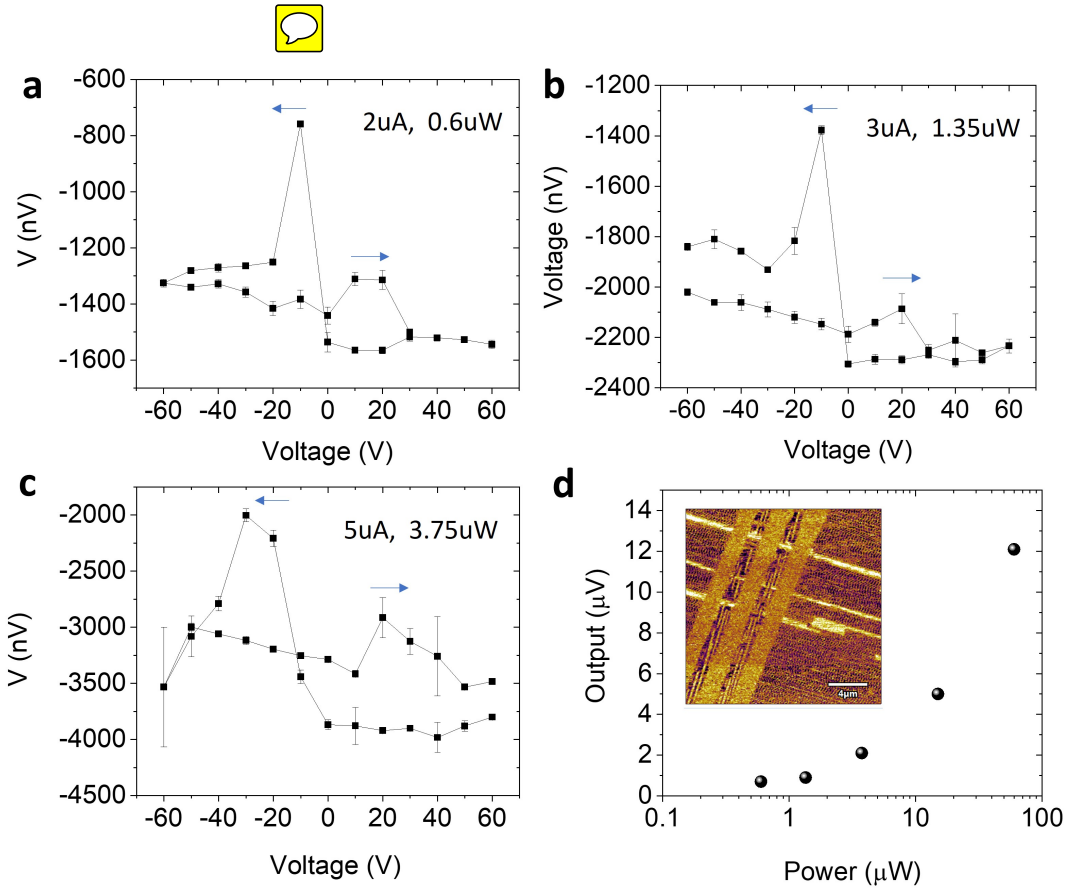
Extended Data Fig. 10. Exchange bias in $BiFeO_3$-based heterostructures. MOKE measurements for LSMO (20 nm)/SIO (10 nm) and LSMO (20 nm)/BFO (25 nm)/SIO (10 nm) samples at room temperature.



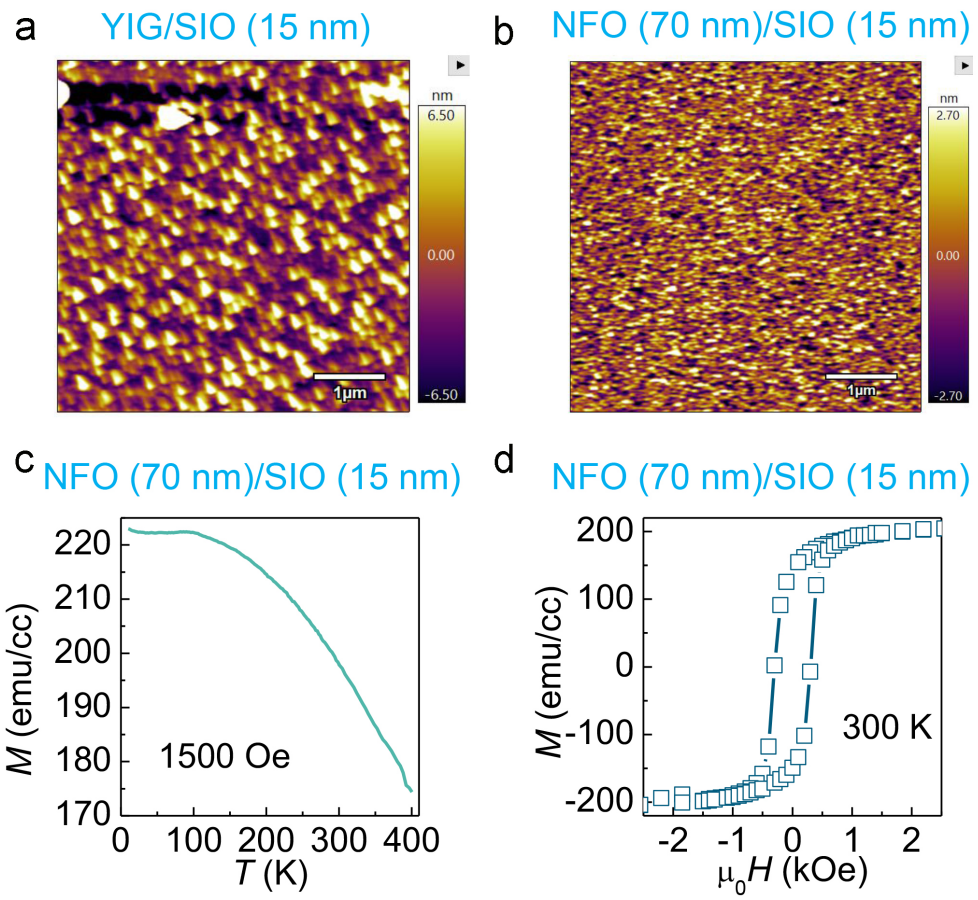
Extended Data Fig. 11. dc non-local voltage as a function of applied magnetic field at room temperature. The applied dc current is 10 μA.



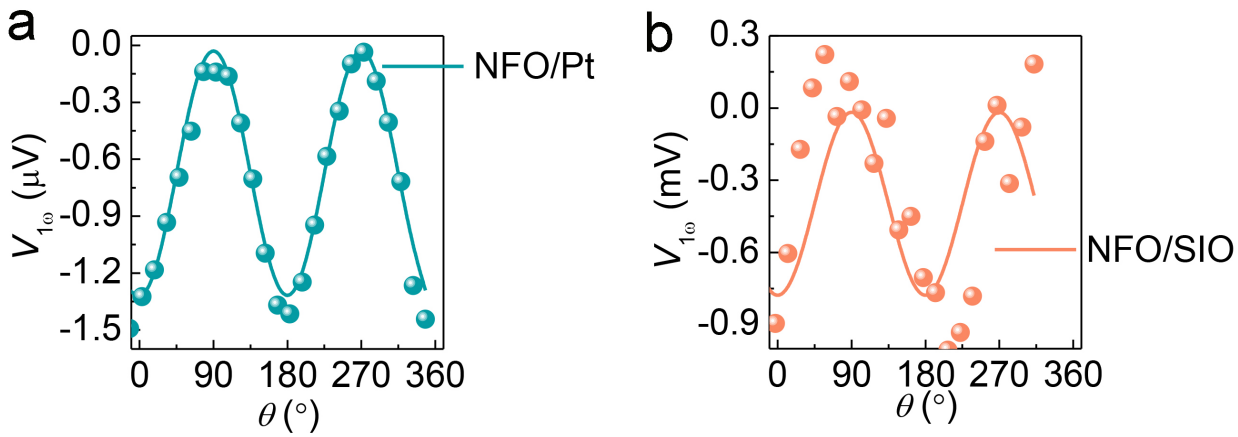
Extended Data Fig. 12. Electric field controlled non-local spin transport measurements with dc current input. A positive electric field of 150 kV/cm and a negative electric field of -300 kV/cm are applied alternately, with dc non-local voltages measured in between the electric fields as shown in the measurement protocol. The corresponding non-local voltage between each electric field is shown below. Each data point is averaged over a time interval of 50 s.



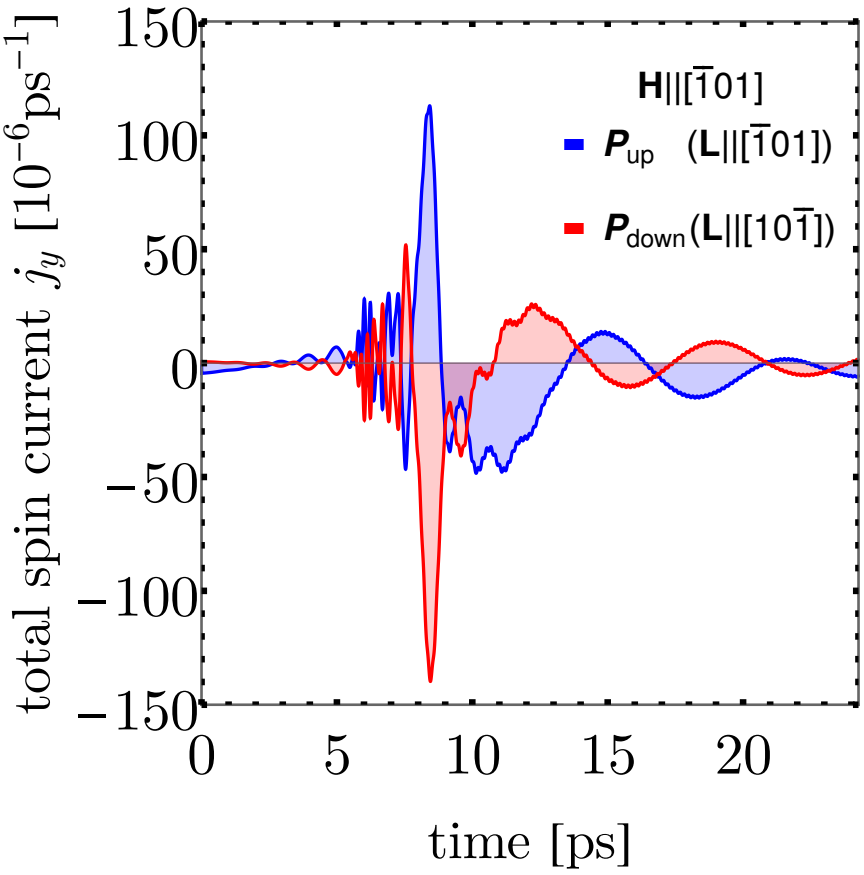
Extended Data Fig. 13. Power-dependent first-harmonic measurements in 71 degree domain BFO. a,b,c, Nonlocal out-put voltage with electric fields (voltage) scan when applying current of 2uA (a), 3uA (b), 5uA (c). d, Summary of power-dependent out-put voltages. Inset shows the PFM image.



Extended Data Fig. 14. AFM and SQUID characterization. a, An AFM image for $SrIrO_3$ (15 nm) grown on YIG/GGG structure. **b,** An AFM image for $SrIrO_3$ (15 nm) grown on $NiFe_2O_4$/STO structure. **c,** Magnetization as a function of temperature from 10 – 400 K, with a magnetic field of 1500 Oe applied in the plane. **d,** Magnetization as a function in-plane magnetic field at 300 K.



Extended Data Fig. 15. Non-local control experiments on $NiFe_2O_4$ (70 nm)/Pt (5 nm) and $NiFe_2O_4$ (70 nm)/$SrIrO_3$ (15 nm). First harmonic voltage signal is displayed in **a** and **b** for $NiFe_2O_4$/Pt and $NiFe_2O_4$/$SrIrO_3$ respectively. An ac current with an amplitude of 100 μA and a frequency of 17 Hz was applied in a channel that is separated by 1 μm from the detection channel.



Extended Data Fig. 16. AFM spin current under L switching. Calculated y-component of the total spin current for up (blue) and down (red) polarization orientations. The applied magnetic field **H** to generate the excitation is set along [$\bar{1}$01]. The Néel vector in both polar configurations is different indicative of a possible 180° switching scenario of **L**. The ratio of the time-integrated *dc* components is +0.978.